AD A 051342

BRL R 2028

M-E 400015

AD

BRL

REPORT NO. 2028

(6) STUDY OF LINER COLLAPSE, JET FORMATION
AND CHARACTERISTICS FROM IMPLOSIVE
SHAPED CHARGE SYSTEMS.

(9) Final rept.,

(10) Abdul R. /Kiwan
Alvin L. /Arbuckle

(14) BRL-2028

(11) Nov 77

(12) 51p.

(16) 1L161102AH43

D D C

MAR 17 1978

Approved for public release; distribution unlimited.

B

(18) SBIE (19) E-400075

(AD)

USA ARMAMENT RESEARCH AND DEVELOPMENT COMMAND
USA BALLISTIC RESEARCH LABORATORY
ABERDEEN PROVING GROUND, MARYLAND

050 750

AD No.
DDC FILE COPY

REPORT DOCUMENTATION PAGE		READ INSTRUCTIONS BEFORE COMPLETING FORM
1. REPORT NUMBER BRL Report No. 2028	2. GOVT ACCESSION NO.	3. RECIPIENT'S CATALOG NUMBER
4. TITLE (and Subtitle) STUDY OF LINER COLLAPSE, JET FORMATION AND CHARACTERISTICS FROM IMPLOSIVE SHAPED CHARGE SYSTEMS		5. TYPE OF REPORT & PERIOD COVERED Final
		6. PERFORMING ORG. REPORT NUMBER
7. AUTHOR(s) Abdul R. Kiwan Alvin L. Arbuckle		8. CONTRACT OR GRANT NUMBER(s)
9. PERFORMING ORGANIZATION NAME AND ADDRESS USA Ballistic Research Laboratory Aberdeen Proving Ground, Maryland 21005		10. PROGRAM ELEMENT, PROJECT, TASK AREA & WORK UNIT NUMBERS 1L161102AH43
11. CONTROLLING OFFICE NAME AND ADDRESS US Army Materiel and Development Readiness Command 5001 Eisonhower Avenue Alexandria, Virginia 22333		12. REPORT DATE NOVEMBER 1977
		13. NUMBER OF PAGES 54
14. MONITORING AGENCY NAME & ADDRESS(if different from Controlling Office)		15. SECURITY CLASS. (of this report) UNCLASSIFIED
		15a. DECLASSIFICATION/DOWNGRADING SCHEDULE

16. DISTRIBUTION STATEMENT (of this Report)

Approved for public release; distribution unlimited.

DDC

MAR 17 1978

B.

17. DISTRIBUTION STATEMENT (of the abstract entered in Block 20, if different from Report)

18. SUPPLEMENTARY NOTES

19. KEY WORDS (Continue on reverse side if necessary and identify by block number)

Shaped charges
Fluid mechanics
Computational methods
Detonation theory

Numerical analysis
Implosion systems
Jets
Shock waves

20. ABSTRACT (Continue on reverse side if necessary and identify by block number) A computational fluid
mechanics study of the detonation, collapse, jet formation, flight and
properties of implosive shaped charge warhead systems. The study shows that a
different liner collapse mechanism occurs from the familiar one of linear and
conical shaped charge systems. The collapse was also seen to deviate from the
ideal conditions initially envisioned. The resulting jet in some cases does
not possess an inverse velocity gradient as in most classical cases. The jet
in this case has distributions of mass, velocity, and energy along its length

DD FORM 1473 EDITION OF 1 NOV 65 IS OBSOLETE

different from those of the classical cases. The different jet characteristics suggest a different type of target interaction than usual. Some of the novel features found numerically were confirmed experimentally. A comparative study of the properties of different types of shape charge warhead designs is also made.

TABLE OF CONTENTS

Page

LIST OF ILLUSTRATIONS

Preceding Page Blank — Film

I. INTRODUCTION

Shaped charge warheads are utilized in a large percentage of military ammunitions. The processes of warhead design, development and testing are rather lengthy, expensive and time consuming. Mathematical modelling and computer simulation of the performance of warhead designs can reduce considerably the amount of proof testing required and eliminate unnecessary development costs. Parametric studies of certain configurations or of proposed design changes can be performed quickly and economically once a basic model has been validated.

Most conventional shaped charge warheads consist of a metallic conical liner with a vertex angle of 30° to 90°, and a cylindrical charge which is molded around it and is point initiated at its end. The resulting detonation wave is approximately planar by the time it strikes the liner and causes the liner to collapse resulting in a low mass high speed jet moving forward and large mass low speed slug moving behind the jet. The mass partition of the different liner elements into jet and slug portions takes place at their respective stagnation points. The theory of jet formation for such warheads was first published in the open literature by Birkhoff, MacDougall, Pugh and Taylor[1] and was later extended by Pugh, Eichelberger and Rostoker[2]. The whole theory was based on simulating the relative motion of the metallic liner during collapse with the steady flow of two jets of water impinging upon each other at the stagnation point. The application of the above theory necessitated assuming the collapse velocity of each liner element or measuring it. Kiwan and Wisnieski enhanced the above theory[3] by calculating numerically the collapse velocities, jet and slug characteristics from the explosive properties and the assumed geometry. They demonstrated the procedure by calculating the properties of two wedge shaped charge liners.

Recent interest has been shown in exploiting other technologies to develop new shaped charge warhead designs for future weapons of the 1980s. In this report we shall investigate some designs of interest and study their characteristics through numerical simulation of their performance. The design shown in Figure 1 consists of a hemispherical metallic copper liner and a hemispherical charge

[1] G. Birkhoff, D. P. MacDougall, E. M. Pugh, and Sir G. I. Taylor "Explosives with Lined Cavities" J. Appl. Phys. 19(1948) p. 563.

[2] E. M. Pugh, R. J. Eichelberger, and N. Rostoker "Theory of Jet Formation by Charges with Lined Conical Cavities" J. Appl Phys. 23, (1951) p. 532.

[3] A. R. Kiwan and H. Wisniewski, "Theory and Computations of Collapse and Jet Velocities of Metallic Shaped Charge Liners" BRL Report No. 1620.

together with an initiation package. The major portion of this study will deal with the hydrodynamic simulation of liner collapse, jet formation, flight and characteristics obtained from the charge shown in Figure 1. Figure 2 shows an idealized schematic of the anticipated liner collapse after being hit by a convergent detonation wave. A typical element E collapses towards the center C with velocity V_c after being hit by the convergent detonation wave. An observer at the pole P sees the element E collapsing towards him with velocity V_r. The liner continually get thicker while it is being compressed, until eventually it starts jetting. The dotted contour shows the actual liner configuration at that time. The equatorial section of the liner is elongating due to the expansion of the detonation products at the unconfined equator.

II. HYDRODYNAMIC CONSIDERATIONS

The hydrodynamic simulation of the collapse, jet formation and characteristics of the above referenced charge is made computationally on the generic charge shown in Figure 3 which does not contain the initiation package referenced in Figure 1. Only half of the charge is shown in Figure 3 due to it being axisymmetric. The HELP code[4] was employed to simulate computationally the performance of the charge shown in Figure 3.

HELP is a two dimensional finite difference multi-material Eulerian code capable of treating compressible fluids and solids in the hydro and elastic plastic regimes. The conservation equations that are solved in HELP are:

$$\frac{\partial \rho}{\partial t} = -\frac{\partial}{\partial x_i}(\rho u_i) \tag{1}$$

$$\rho \frac{Du_i}{Dt} = -\frac{\partial}{\partial x_i}(\sigma_{ij}) \tag{2}$$

$$\rho \frac{DE_T}{Dt} = \frac{\partial}{\partial x_i}(\sigma_{ij}) \tag{3}$$

where x_i denotes the ith Coordinate of position, t the time, ρ denotes the density, u_i the ith velocity component, E_T the total energy. $\frac{D}{Dt}$ stands for the total material derivative, σ_{ij} is the stress tensor

---

[4] L. J. Hageman et al., "HELP A Multi-material Eulerian Program for Compressible Fluid and Elastic - Plastic Flows in Two Space Dimensions and Time" Systems, Science and Software Report 75-2654 (1975).
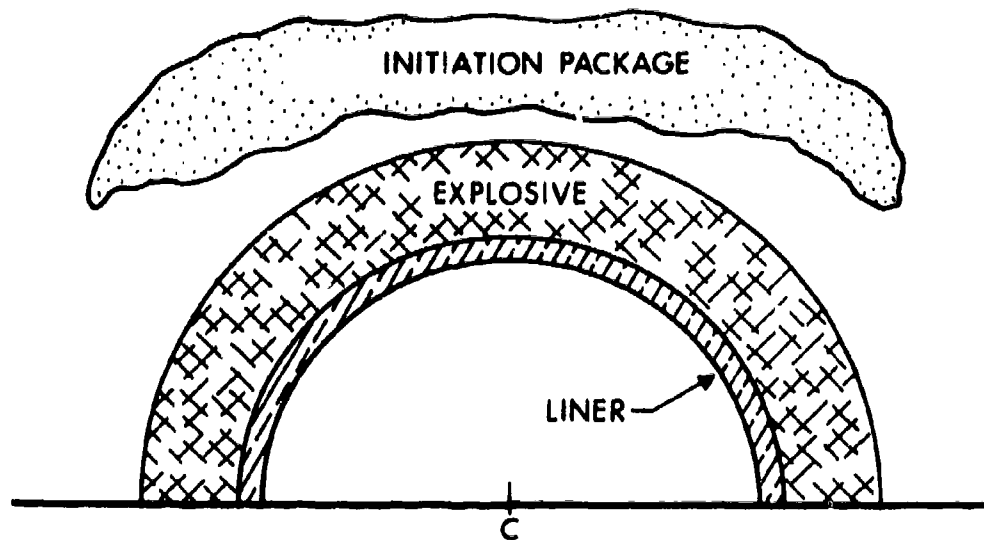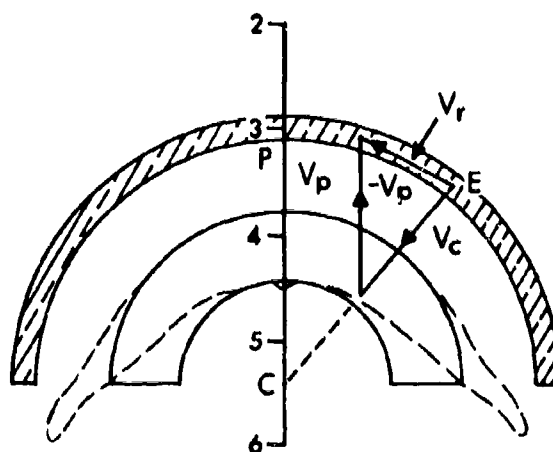
8

Figure 1. Schematic of a Shape Charge Warhead

Figure 2. Idealized Schematic of Imploded Hemisphere Collapse
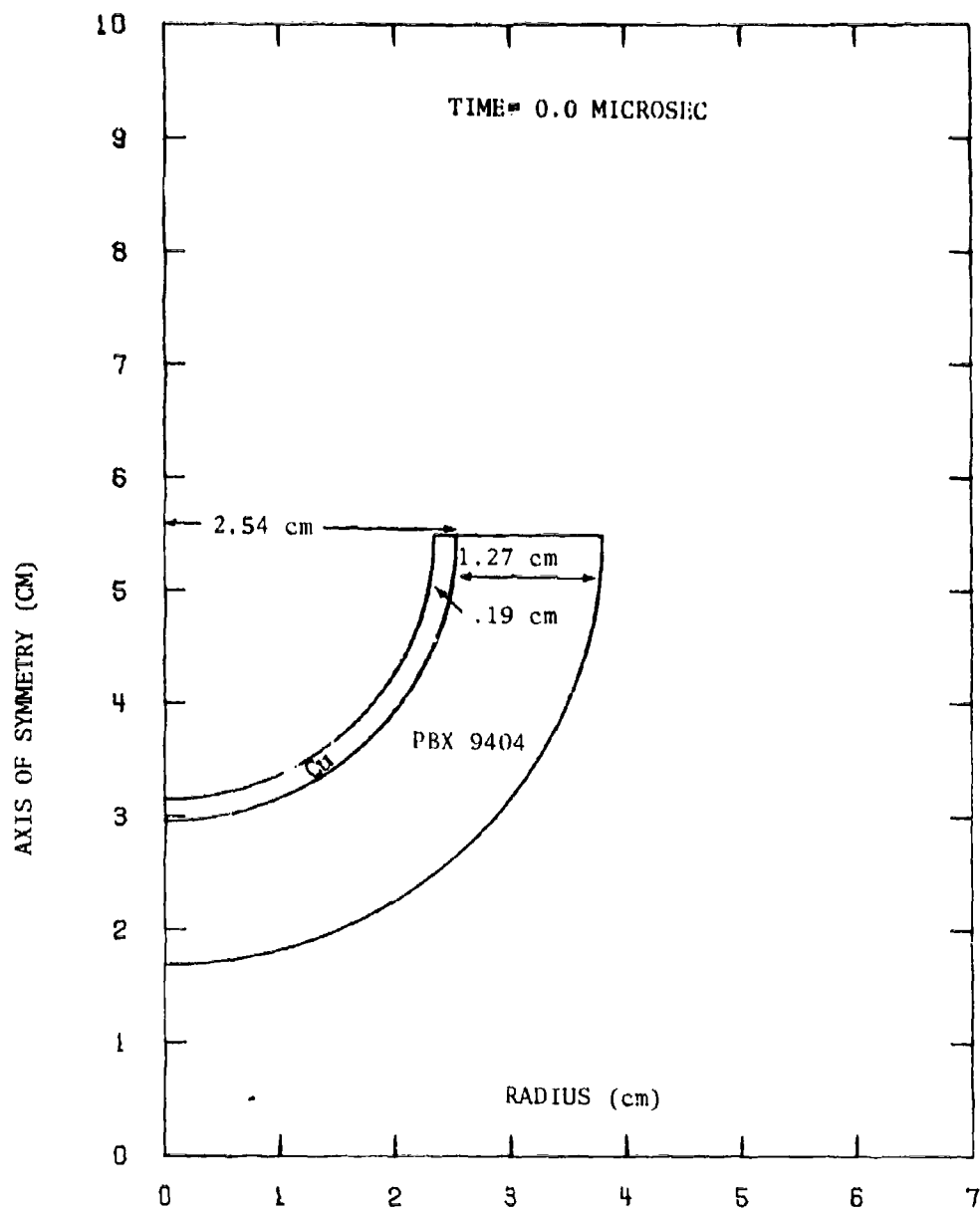
Figure 3. A Schematic of the Computational Setup

which can be separated into its hydrostatic stress component (pressure) $-\delta_{ij}p$, and a stress deviator tensor S_{ij}, i.e.,

$$\sigma_{ij} = S_{ij} - \delta_{ij}\,p \qquad (4)$$

Equations (1), (2) and (3) are transformed into conservation form[5] and then put into an equivalent integral form before applying finite difference methods to these equations. The equations that are therefore solved by finite difference methods for each cell of the computational mesh and every computational cycle are:

$$\Delta m = -\Delta t \int_S \rho u_i n_i \, dS \qquad (5)$$

$$\Delta(m\,u_j) = \Delta t \int_S S_{ij} n_i \, dS - \Delta t \int_S p u_j \, dS - \Delta t \int_S \rho u_i u_j n_i \, dS \qquad (6)$$

$$\Delta(mE_T) = \Delta t \int_S S_{ij} u_j n_i \, dS - \Delta t \int_S p u_i n_i \, dS - \Delta t \int_S \rho u_i E_T n_i \, dS. \qquad (7)$$

n_i denotes the unit vector normal to a surface element dS.

Equations (5) through (7) are supplemented by appropriate initial and boundary conditions to initiate the flow. Material properties are represented in HELP by the Tillotson Equation[6] of state for inert materials, the ideal gas equation of state, and the JWL equation of state for explosion products. The code also contains a burn routine based on the JWL Equation of state. The above flow equations are integrated in three phases corresponding to the evaluation of the three different types of integrals occuring in these equations and called the SPHASE (Strength phase), the HPHASE (Hydro phase), and the TPHASE (Transport phase).

HELP contains a variety of options such as transmittive and reflective boundary conditions at various grid boundaries. It contains also an artificial viscosity option. Material interfaces are defined in Lagrangian manner and are identified by massless tracer particles. A slide line can also be introduced along a material interface separating two materials which permit them to slide against each other.

---

[5]P. D. Lax, "Weak Solutions of Nonlinear Hyperbolic Equations and Their Numerical Computation", Comm. on Pure and Applied Math, Vol III, p 159 - 193, (1954).

[6]J. H. Tillotson, "Metallic Equations of State for Hypervelocity Impact," General Atomic Report GA-3216 (1962).

11

Although HELP models the strength properties of materials and contains a yield criterion and a failure criterion our calculations will be restricted to the hydrodynamic phase, with only viscous effects incorporated. Our experience with calculations incorporating the SPHASE of the code is limited, and we have not investigated the validity of the model used in that part of the HELP code. Walsh[7] reported that the results of his calculations using the HELP code in similar problems were not significantly affected when the strength effects were incorporated.

III.   COMPUTATIONAL SET UP AND SIMULATION

The computational simulation of the performance of the charge shown in Figure 3 was made in a computational mesh of 50 x 90 cells. Each cell was 0.8 mm x 0.8 mm in the region containing the metallic liner whose thickness is 1.9 mm. The zones were gradually enlarged radially and axially to the end of the mesh. The choice of the mesh size had to be balanced between the desire for accuracy of the solution obtained and the speed of the computations. A coarse mesh size is detrimental to the accuracy of the calculations particularly so if any material region consisted of mixed cells only. A fine mesh enhances the computational accuracy but requires a larger mesh and reduces the magnitude of the time step and thus requires longer computational time to solve a given problem. Ten equally spaced latitude circles (initiation rings) were selected on the outer hemispherical surface of the charge shown in Figure 3. The simultaneous initiation of these rings was considered to simulate reasonably well the initiation process of the actual charge.

Figure 4 shows the liner configuration at t=1.92 μs together with the velocity field. The liner is seen starting to collapse after being hit by the almost convergent detonation wave about 0.46 μs earlier. The lack of confinement on the equatorial plane allows the detonation products to expand rapidly from that surface causing a departure from the idealized collapse depicted in Figure 2. The equatorial section of the liner starts to elongate at the explosive-metal-air-interface. As the equatorial rarefaction wave travels along the surface of the liner towards the polar region the pressures and velocities are reduced. Figure 5 shows the pressure in the flow field which is found to be large and rising in the collapsing liner where it has a maximum value of 0.328 Mbar. About that time (t=1.92 μs) the effect of the rarefaction from the nearest unconfined spherical surface of the charge starts to be felt at the liner surface and the pressure begins to decrease. Figure 6 shows the flow field at t=5.8 μs. The liner is observed to be getting thicker at the pole and elongating further in the equatorial region. The pressure field is seen in Figure 7 to have

---

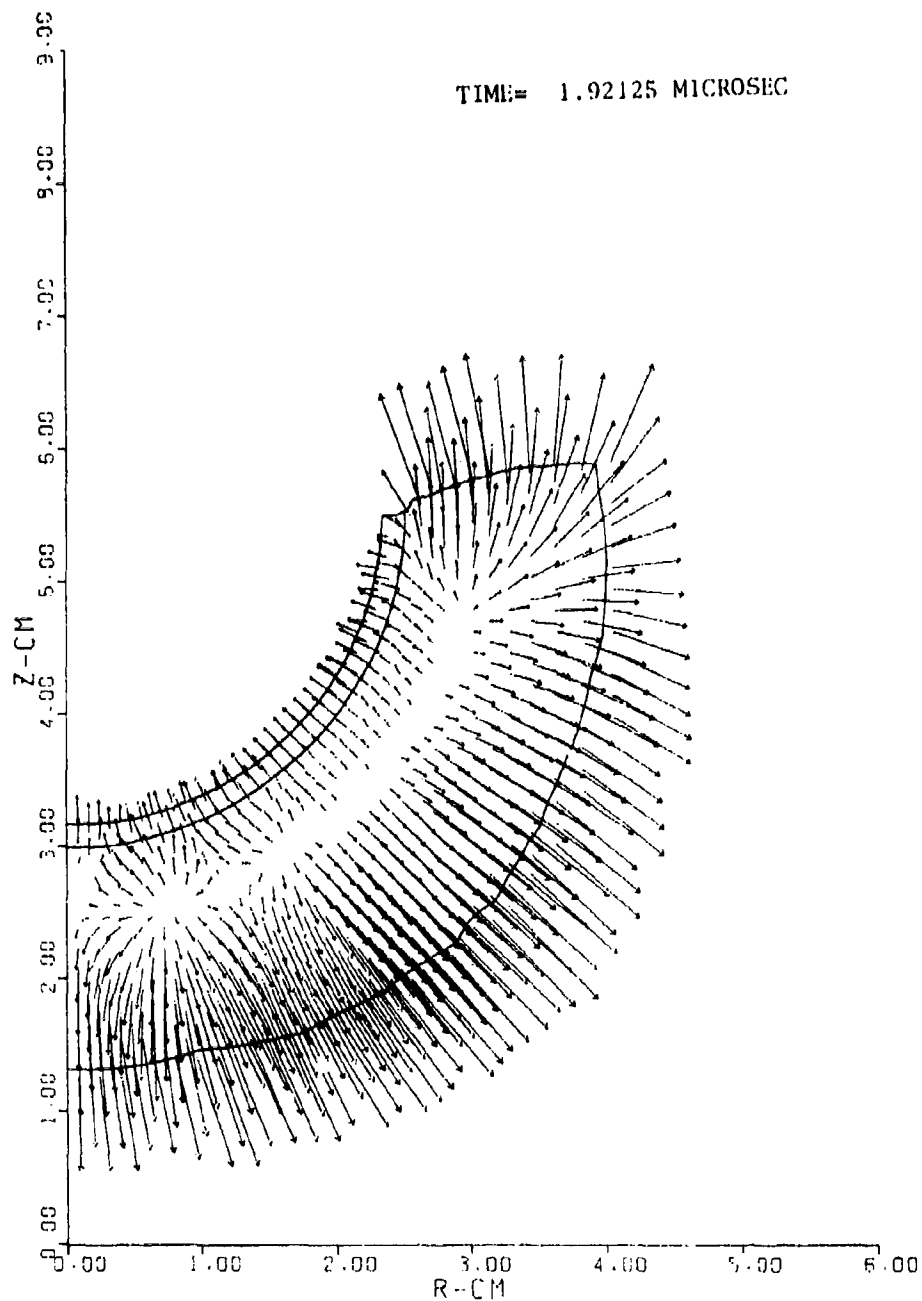[7]*J. M. Walsh, private communication.*

12

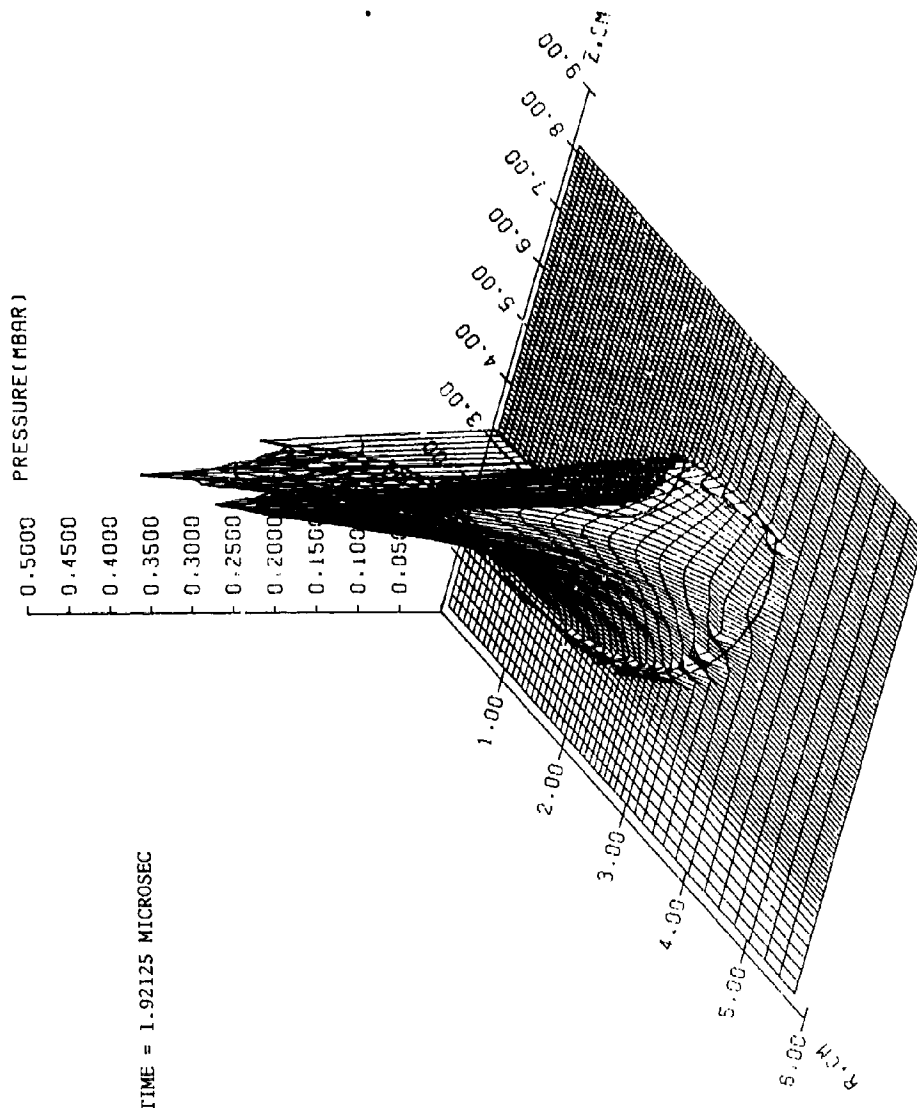Figure 4. Configuration and Velocity Field Shortly After Detonation
Wave Strikes Liner

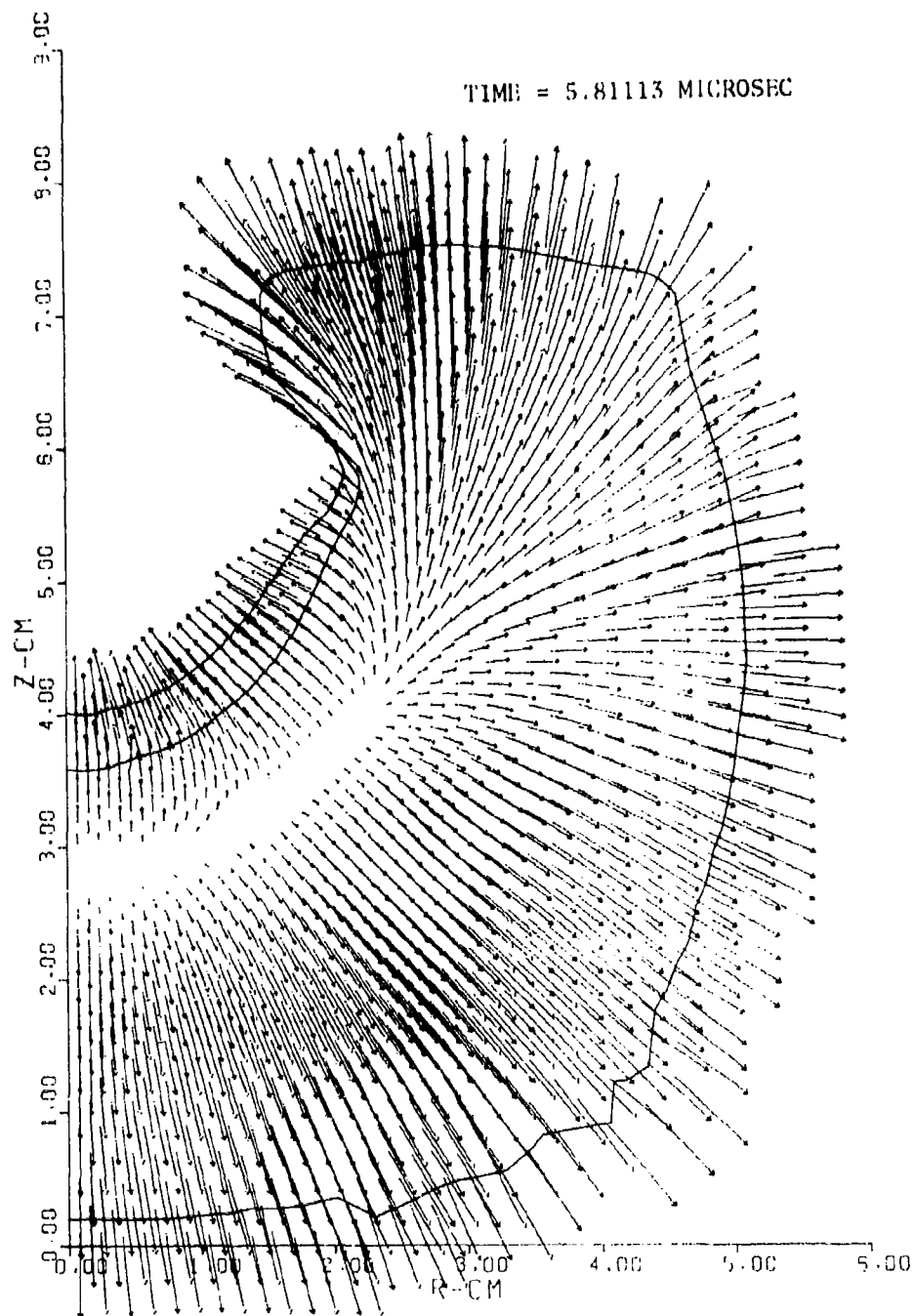13

Figure 5. Pressure Field at an Early Stage

14

Figure 6. Flow and Velocity Fields Shortly Before Jet Formation

15

PRESSURE (MBAR)

0.1600
0.1400
0.1200
0.1000
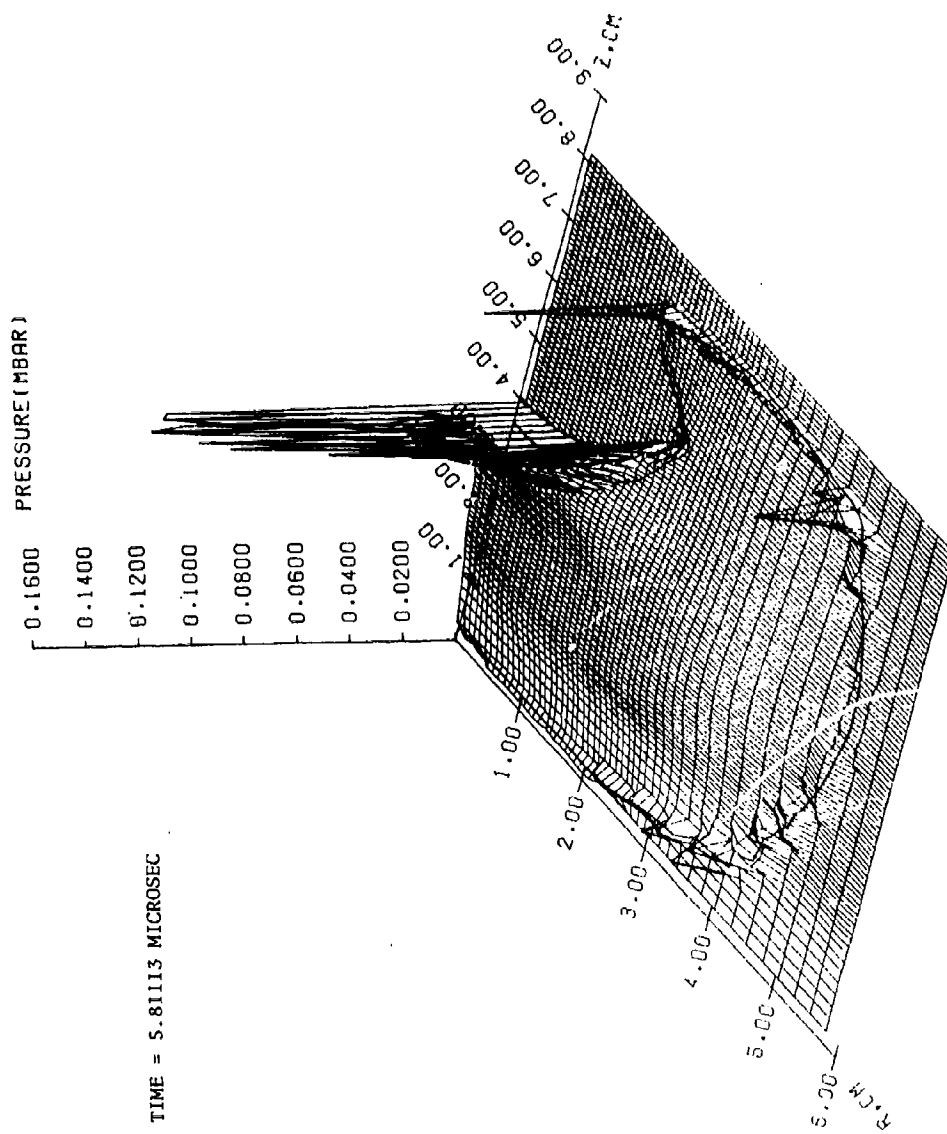0.0800
0.0600
0.0400
0.0200

TIME = 5.81113 MICROSEC

Figure 7.   Reduced Pressure Field Due to Nonconfinement

16

decreased significantly by that time. The maximum pressure in the
liner material is found to be 0.15 Mbar. As the liner collapse
advances, the pressure starts to increase again due to liner com-
pression and reaches a maximum value of 0.603 Mbar, at t=9.2 μs
as can be seen in Figure 8. The pressure decreases thereafter due
to the influence of the equatorial rarefaction and the expansion of
liner material arising from jet formation and elongation. The
rarefaction wave emanating from the equatorial plane reaches the polar
region about t=7.2 μs and the jet becomes distinguishable after that
time. Figures 9 and 10 show the early stages of jet formation. The
short arrows show the direction of the local flow velocity in the differ-
ent layers of liner material. Figures 11 through 13 show the late
stages of jet formation and flight. A particularly remarkable feature
in those Figures is that the equatorial section of the liner impacts
the jet after its initial elongation. Several other features of these
jets will be discussed more fully later. Figure 14 shows a plot of the
velocity versus time for ten different tracer particles placed on the
inside surface of the hemispherical liner, while figures 15 through 17
show plots of velocities versus time of four particles placed across the
liner thickness at three different locations, one on the axis of symmetry
and the others are placed at locations whose radii make angles of 36°
and 72° respectively with the axis of symmetry.

IV. RESULTS AND EXPERIMENTAL COMPARISON

The primary advantage of mathematical modelling and computational
simulation of physical problems is the wealth of information available
once a successful model has been achieved. The values of the various
calculated physical parameters of the problem are available throughout
the region of computation in a permanent record form which can subse-
quently be retrieved and examined. Parametric studies can also be made
quickly and sometimes economically. In this section we shall summarize
our computational results and compare them with some of the available
experimental data. Figure 18 shows a plot of the average velocity
components of the metallic liner as a function of time, while Figure 19
shows the different liner energies as functions of time. The initial
rarefaction wave arriving at the liner surface due to the nonconfinement
of the spherical charge surface reduces the liner acceleration, while
the equatorial rarefaction wave causes the jet to become distinguishable.
The continued liner compression converts the liner radial momentum to
axial momentum. The total liner energy increases rapidly at first and
approaches an asymptotic value later on. Figure 20 shows a plot of
jet velocity as a function of cumulative mass at various times. The
jet mass continually increases as more metal is accelerated to jet
velocities.

17

It was found numerically that about 18.7% of the hemispherical liner forms the jet (i.e., has velocity $\geq$ 2mm/µs). Experimental measurements estimate the jet mass to be about 18% of the liner mass. The calculations indicate that about 19.9% of the explosive energy is delivered to the copper liner of which 11.8% is in kinetic energy form and 8.1% is in internal energy form. The kinetic energy of the jet is 41% of the total energy of the liner (69% of the kinetic energy of the liner). The jet tip velocity was found to be 6.42mm/µs. Two experimental measurements of jet tip velocity were made at BRL of 7.07mm/µs and 7.57mm/µs. In the experimental tests the hemispherical charge used was 0.151 kg of PBX and the initiation package contained 0.2685 kg of composition B-3. In the computations only the energy from the hemispherical charge was incorporated in the calculations.

If one adds the kinetic energy of the flier plate, in the initiation package, to the explosive energy of the charge then the resulting jet velocities will increase on the average by about 8%. The resultant jet tip velocity will increase to 6.92mm/µs. If in addition one considers the effect of the confinement provided by the flier plate and scale the jet tip velocity according to the values given in columns (a) and (e) of Table 1 of this report, the jet tip velocity will be found to be 7.35mm/µs which is within the range of experimental measurements.

Several important observations can be made from the computations, concerning the jet properties from such systems. No inverse velocity gradient was found in the jet produced by such systems as in the case of most conical systems. The lead particle in the jet has as a result of this a small amount of mass. Examination of Figures 9 and 10 suggests that the jet forms from the liner material located on the inside surface layer of the liner, while the remaining liner material ends up in the slug. This observation is confirmed from an examination of the velocity plots shown in Figures 14 through 17. Figure 14 shows that the entire inside surface layer of the liner reaches terminal jet velocities except for the equatorial portion of that layer. Figures 15 through 17 confirm this observation. The amount of jet mass and kinetic energy from such a system is similar to that obtained from conical systems (same order of magnitude), although their distributions along the jet length appear to be different. X-rays from early experimental tests showed a part of the jet to be missing. It was thought at the time that that part of the copper jet vaporized. The calculations shown in Figures 11 and 12 show the correct interpretation. It is clear from those figures that the equatorial portion of the hemispherical liner after initially stretching, moves inwards and pinches off the jet. X-rays of the jet at early times were then taken in subsequent test firings which confirmed the theoretical predictions. Figure 21 shows the jet obtained from one of the experimental test firings. The equatorial protion of the liner is seen in the process of pinching off the jet.
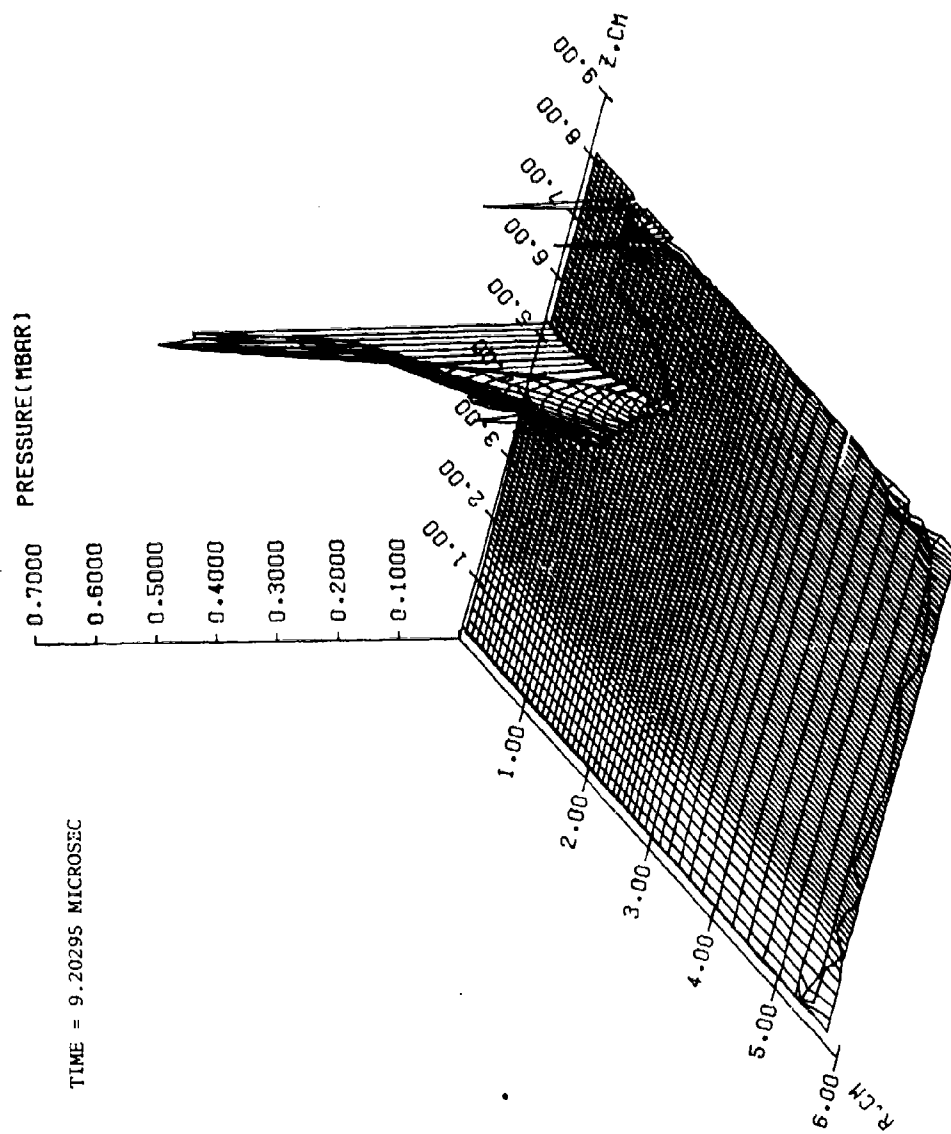
18

TIME = 9.20295 MICROSEC

PRESSURE(MBAR)

0.7000
0.6000
0.5000
0.4000
0.3000
0.2000
0.1000

Figure 8.   High Pressure in Liner Due to Compression
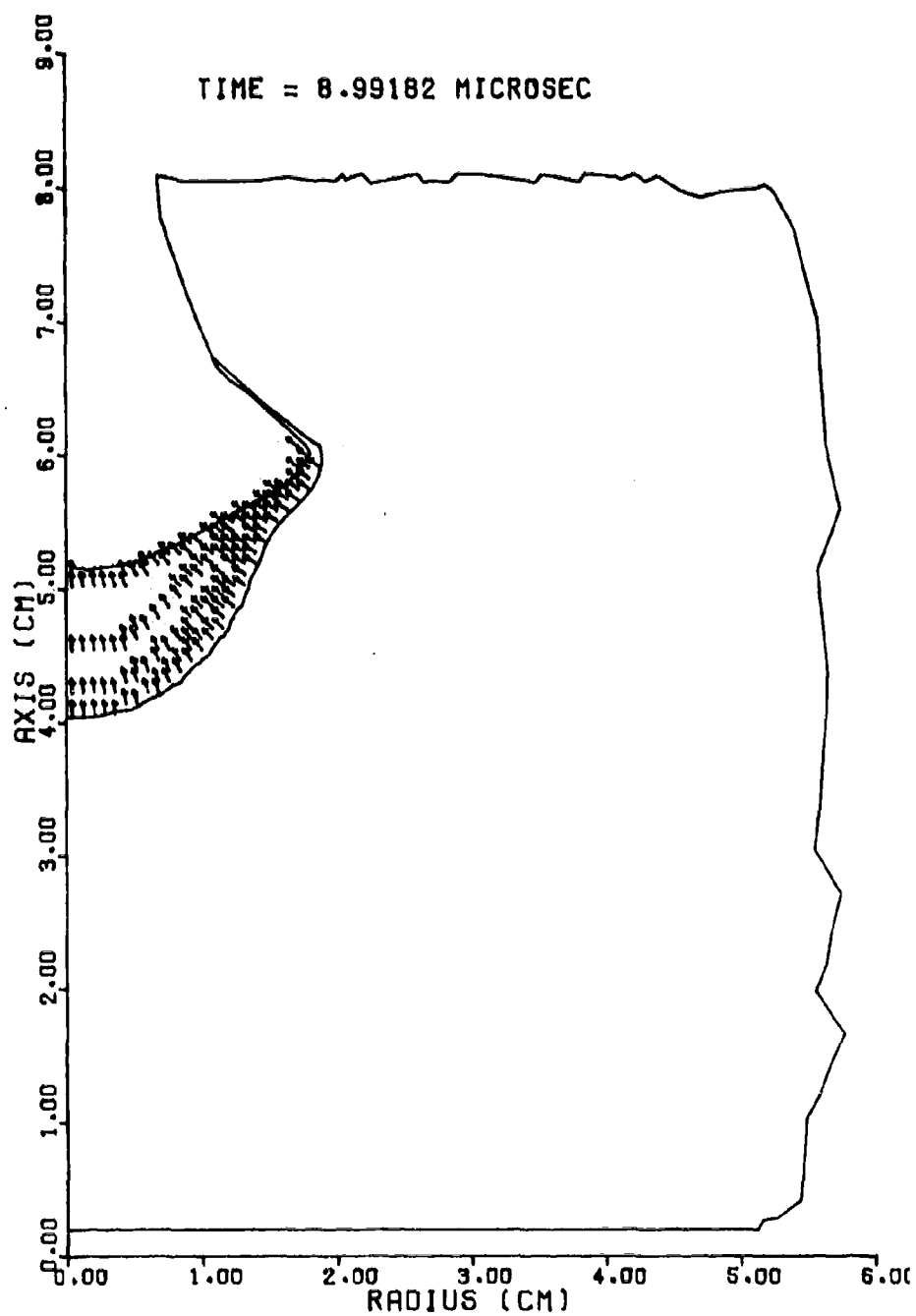
Figure 9. Early Stage of Jet Formation

20

TIME = 11.64562 MICROSEC
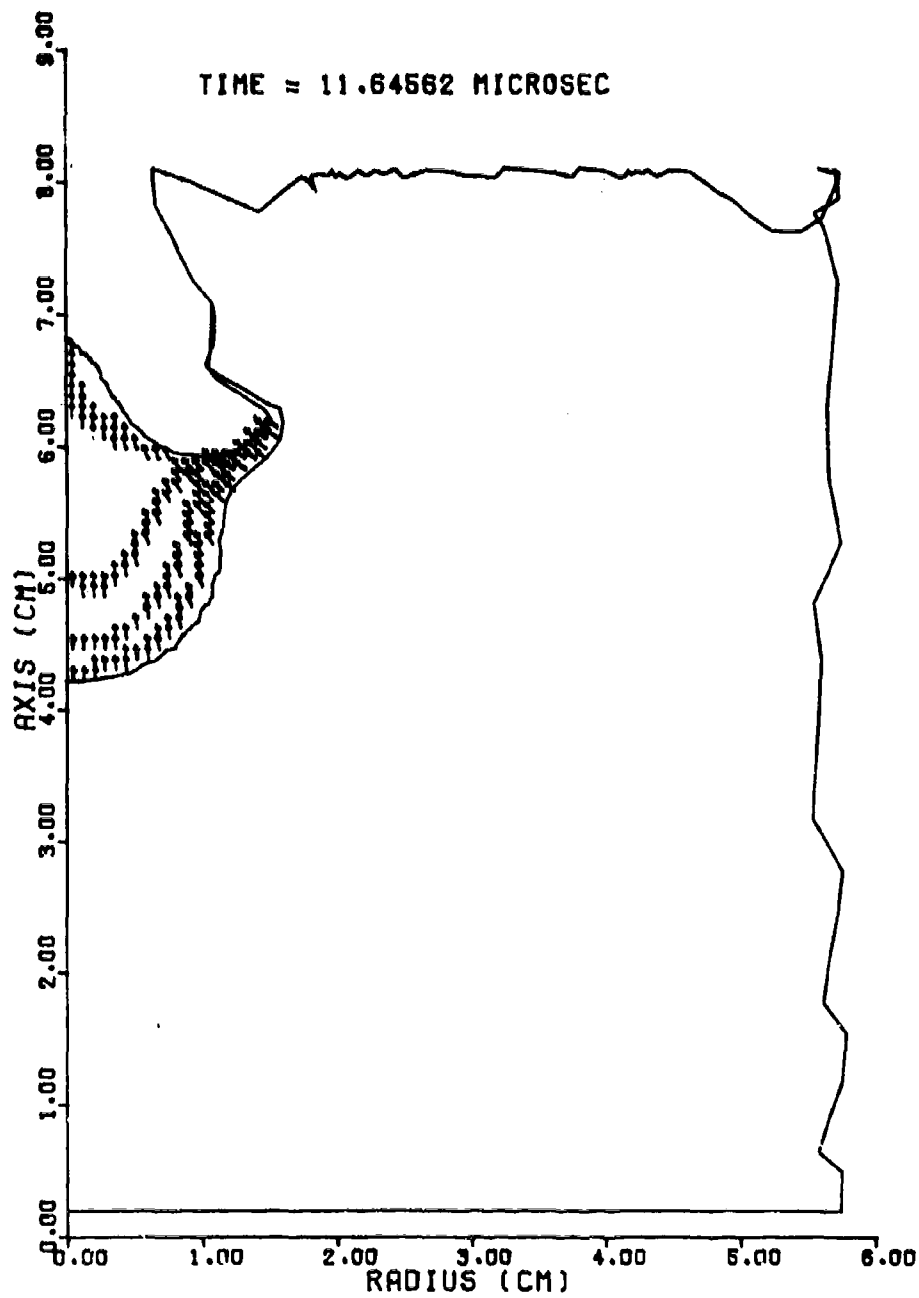
Figure 10. Early Stage of Jet Elongation

21

TIME = 17.71877 MICROSEC
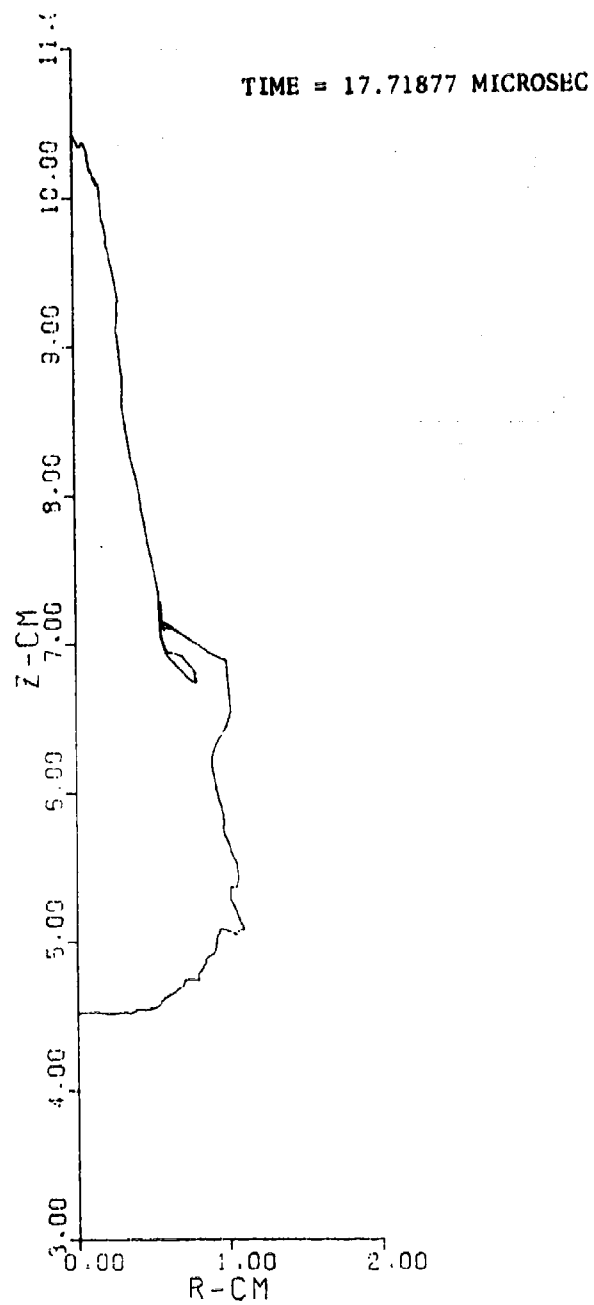
Figure 11.   Early Stage of Jet Flight

22

TIME = 22.67634 MICROSEC
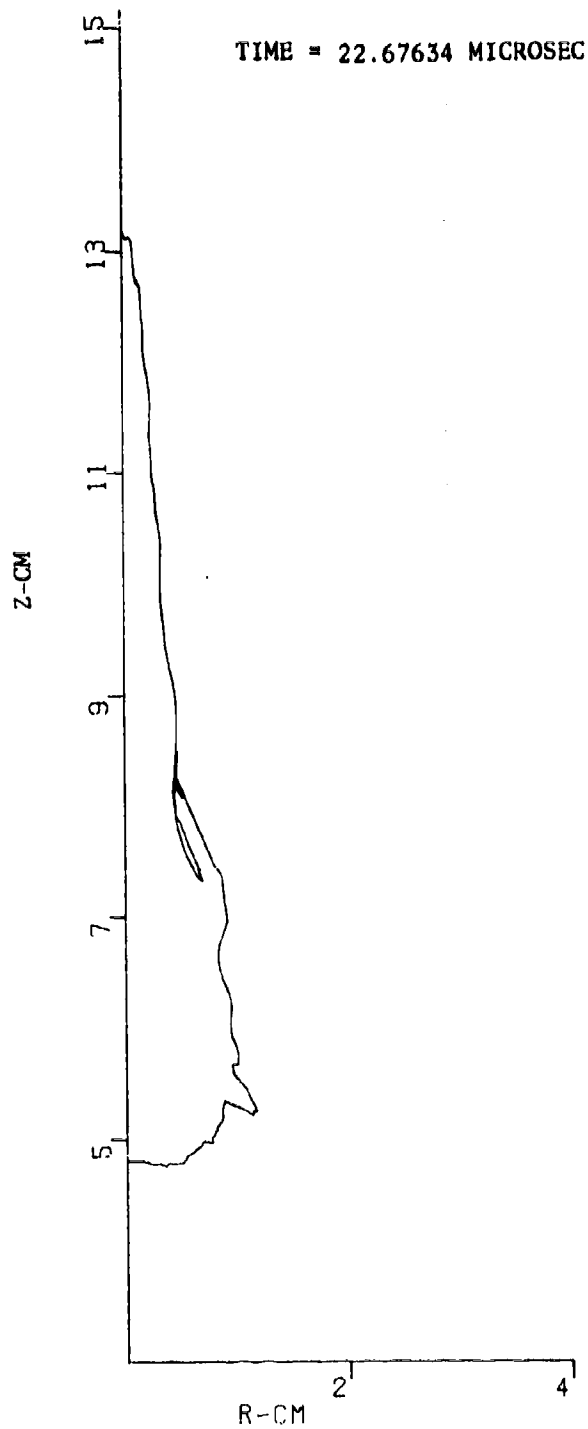
Figure 12.   Jet Elongation and Flight

23

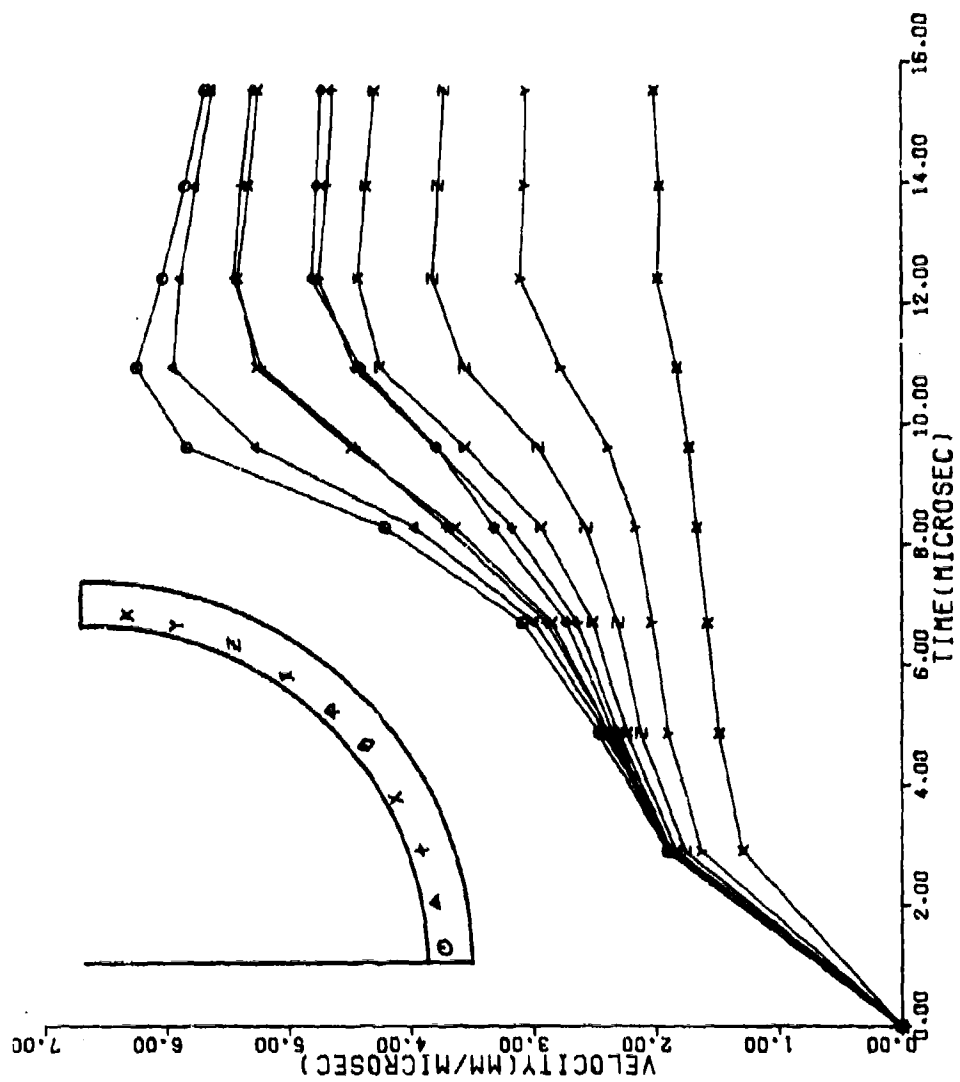TIME = 39.90044 MICROSEC
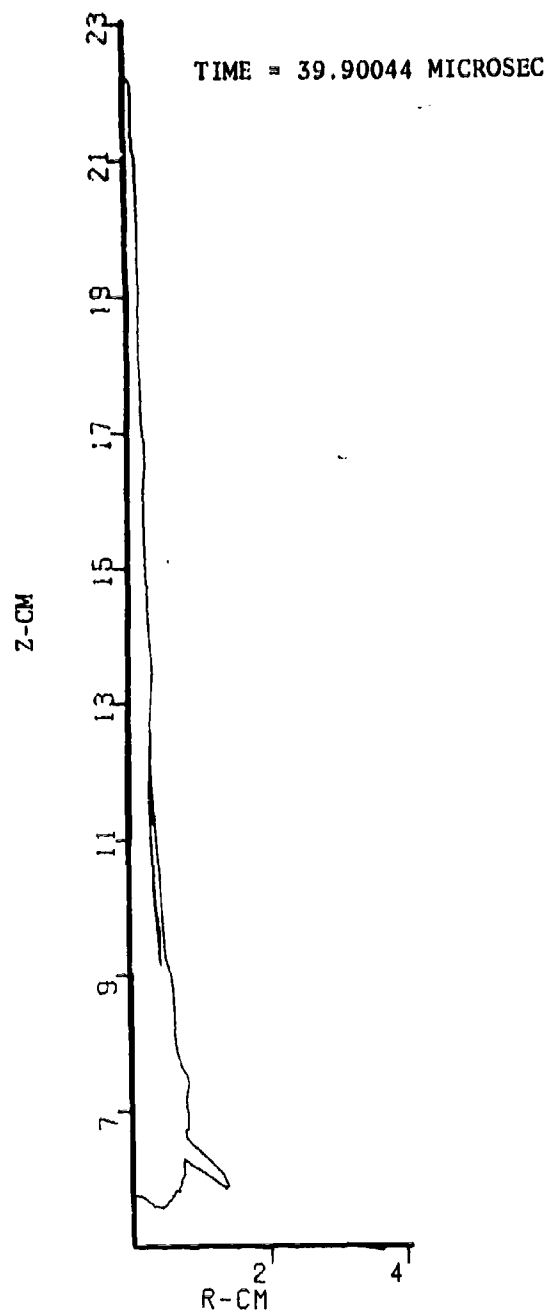
Figure 13.   Late Stage of Jet Configuration

24

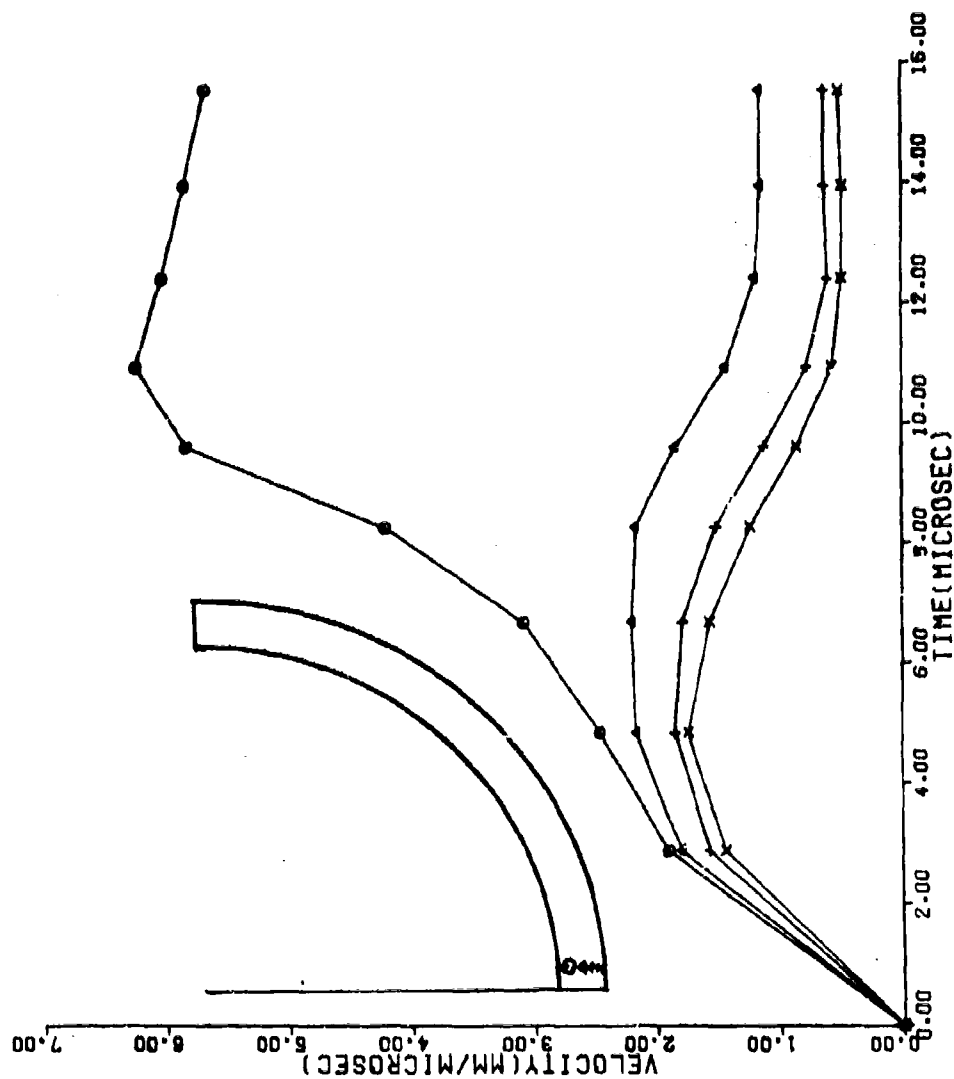Figure 14. History of Velocities of Tracer Particles Placed on Inner Liner Surface

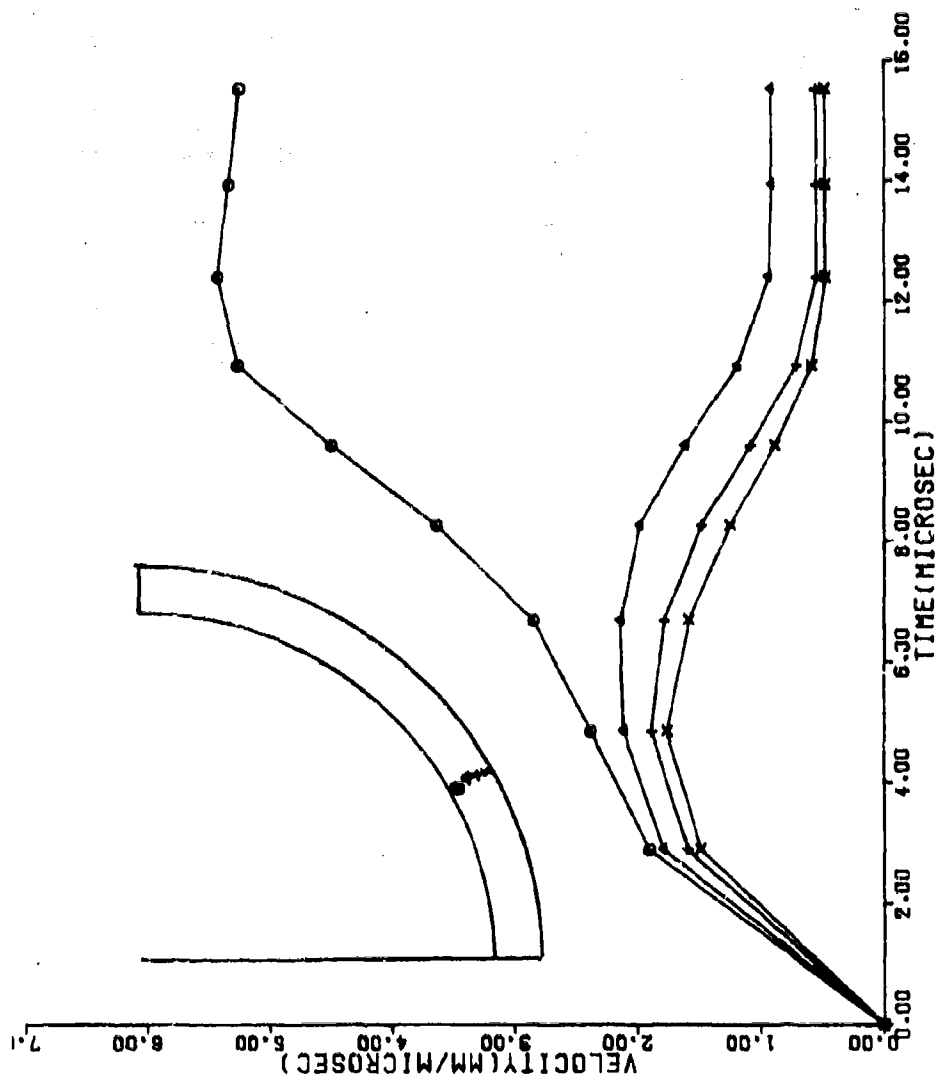Figure 15. Velocity Versus Time of Tracers on Axis of Symmetry

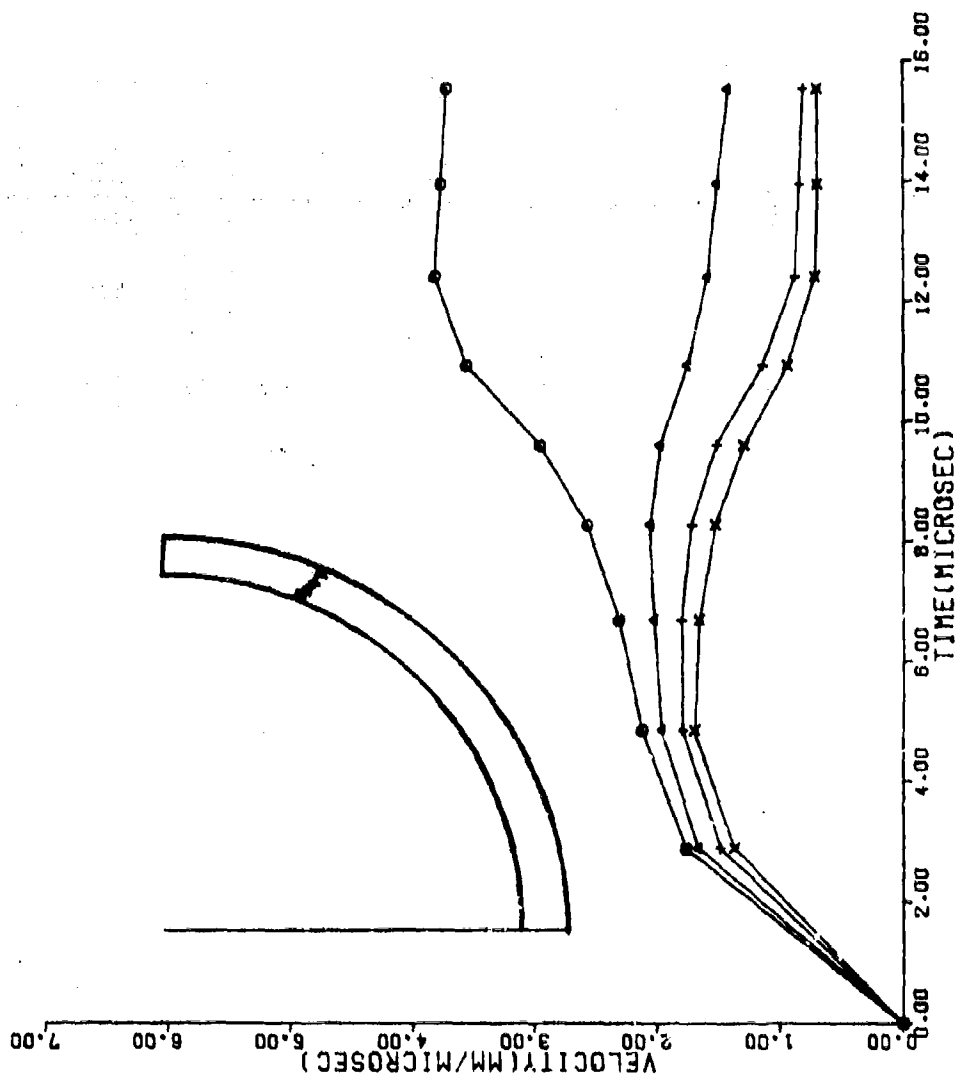Figure 16. Velocity Versus Time of Tracers 36° off Axis of Symmetry

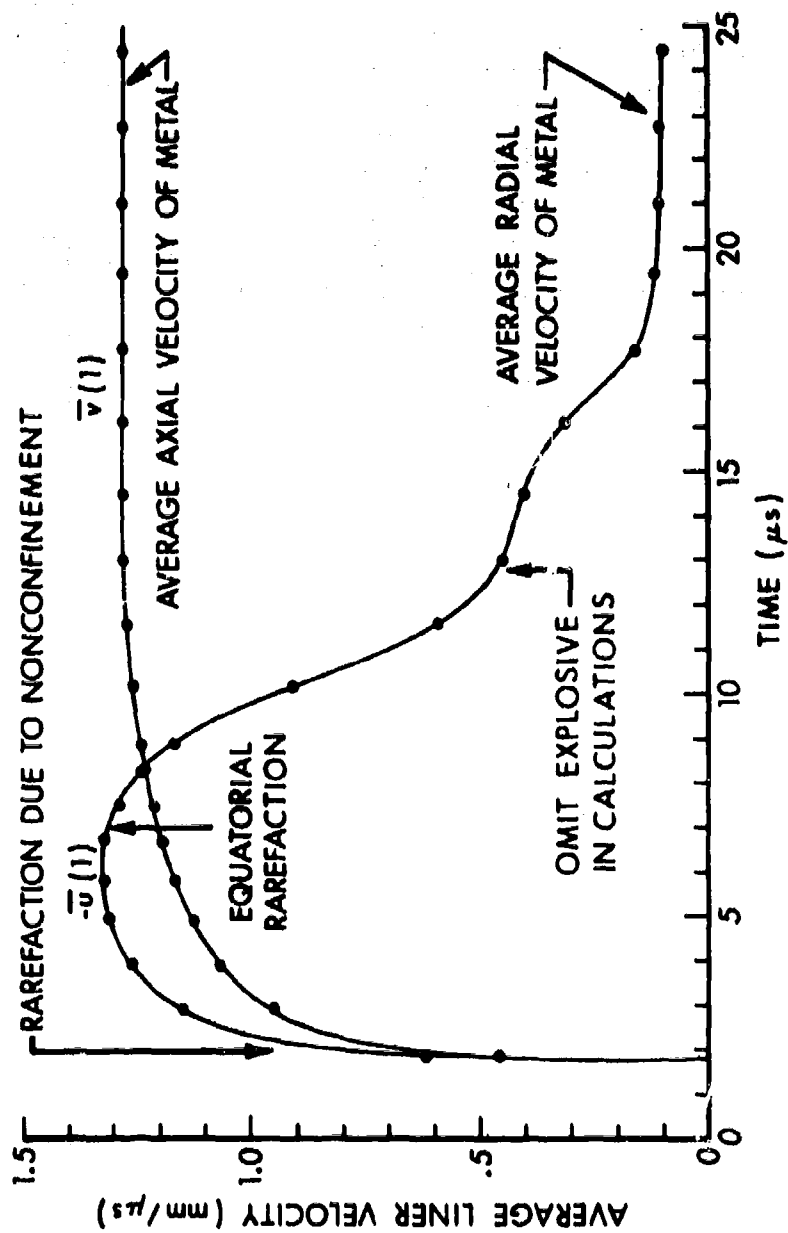Figure 17. Velocity Versus Time of Tracers 72° off Axis of Symmetry

28

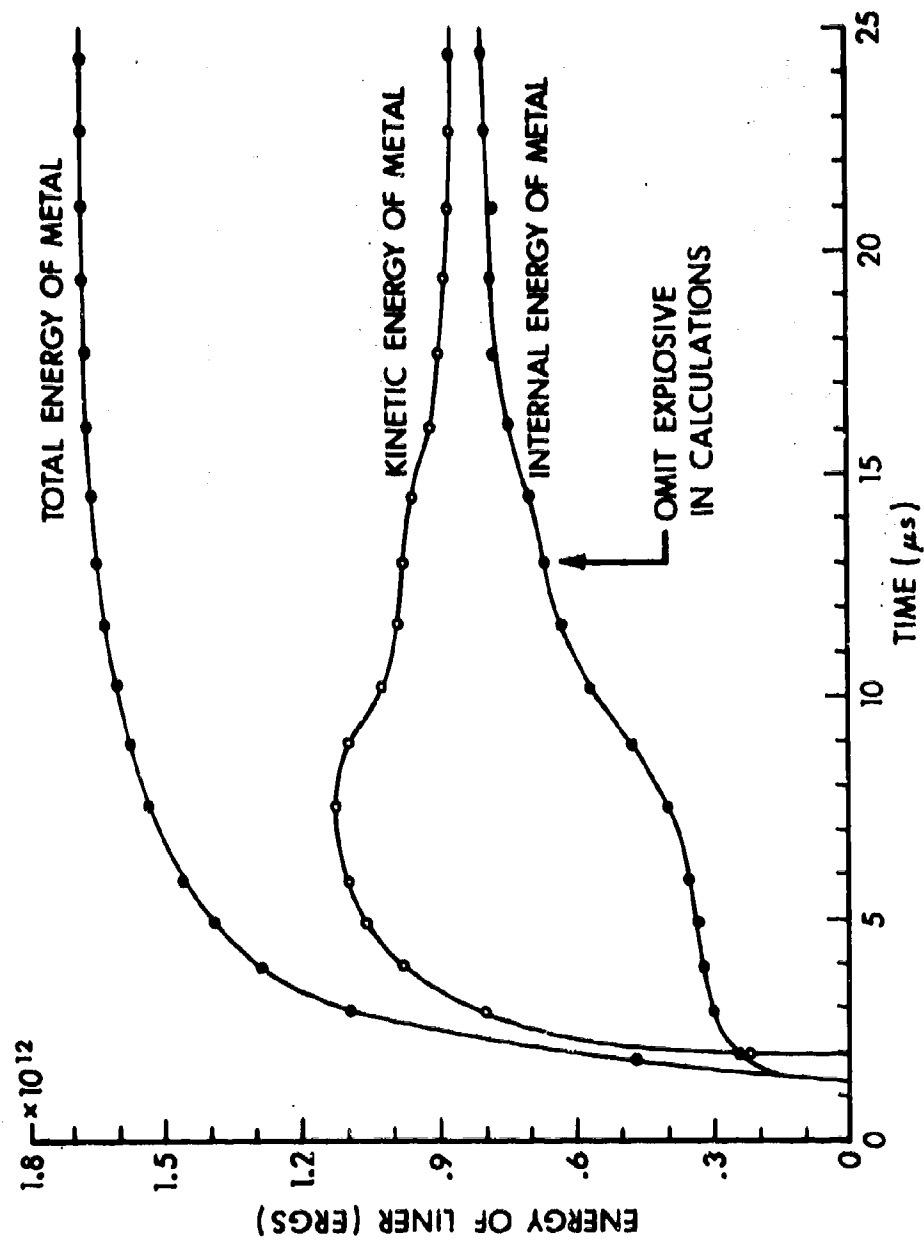Figure 18. Histories of Average Velocity Components of Copper Liner
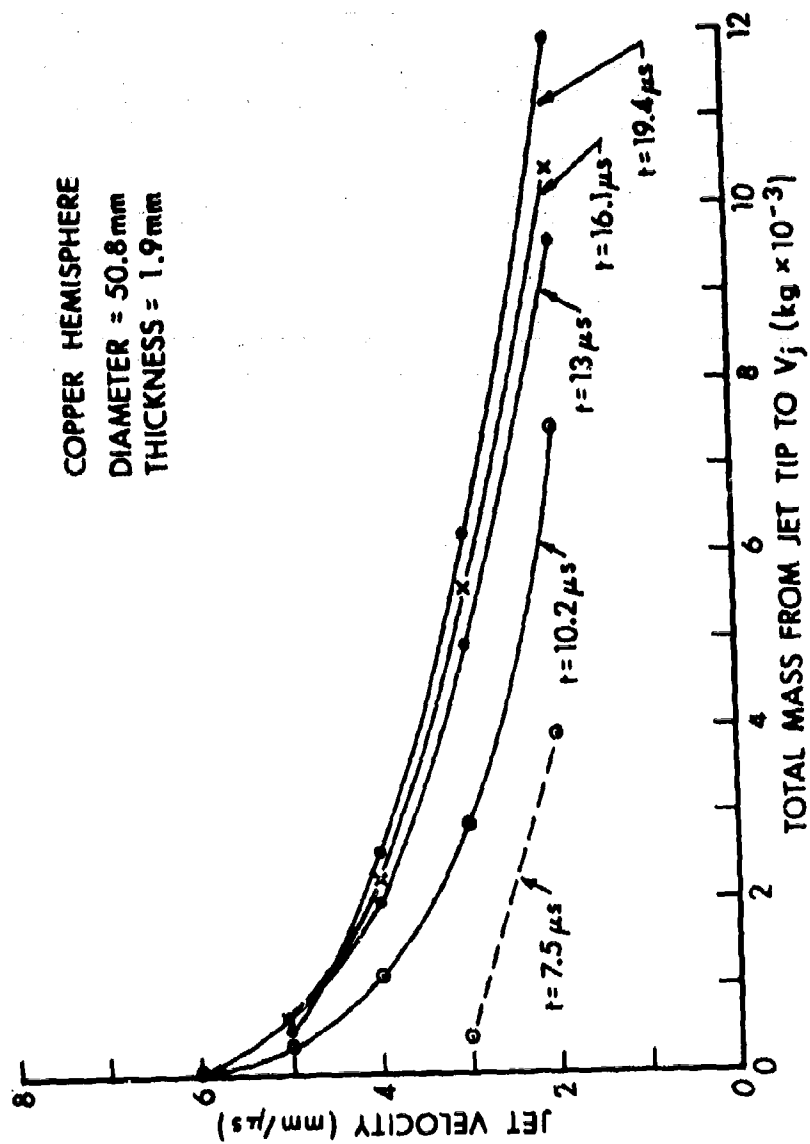
Figure 19. Histories of Liner Energies

30

Figure 20. Jet Velocity vs. Cummulative Mass of Copper Liner

31

Figure 21.   View of Jet Being Struck by the Liner Equator at 17 Microsec

V. COMPARISON OF DIFFERENT DESIGN CONFIGURATIONS

The above numerical study dealt exclusively with the hemispherical liner collapse under implosion and the jet obtained from the shaped charge configuration shown in Figure 22(a). In this section we shall compare briefly the collapse and jet properties of the charges shown in Figures 22(b) through 22(f) with the above studied charge 22(a).

The charge shown in Figure 22(b) is cylindrical in shape, contains the same mass of explosive as the previous case, but is initiated at its end by a plane wave. Figure 23 shows the computational setup, while Figure 24 shows the plane detonation wave at t = 2.2μs shortly before striking the liner. Figures 25 and 26 show the early stages of the liner collapse in this case. Figures 27 and 28 show the early stages of jet formation for this case, while Figures 29 and 30 show the late stage jet configurations.

It is apparent from examining Figures 23 through 30 and the rest of the computational plots (not shown) that the liner turns inside out in this case. The resulting jet from this shaped charge design, which is defined to be that part of the collapsed liner with velocities $\geq$ 2mm/μs, is seen to be a short thick jet. Some instability is seen to occur near the base of the slug. The jet takes a longer time to form, its mass is about the same as the previous case 22(a) (11.6 x10^{-3}kg), but is considerably slower moving, the jet tip velocity being only (3.6mm/μs). The total energy communicated to the liner is (8.9 x 10^{4}J) which is about 52% of the energy communicated to the liner in the previous case 22(a). Figure 31, views (a) through (c), show the jet obtained experimentally from a copper hemisphere whose radius is 1.9 cms with a cylindrical charge which is point initiated at its end along the axis of symmetry. Figure 31(d) shows our computational prediction of the liner configuration at t = 28.7μs after initiation for the charge shown in Figure 22(b) with a plane wave as described above. The similarity between the experimental and computational results is encouraging and provides some validation of our computational model.

The charge shown in 22(c) is similar to 22(a) except that some of the explosive in the equatorial region was shaved off in the hope that the equatorial portion of the liner will take a longer time before it interrupts the jet. The interruption of the jet was delayed about 6μs, but it was not possible to eliminate it. The jet obtained in this case was similar to that obtained from 22(a). Table 1 contains the characteristics of the jets obtained from charges 22(a) through 22(f), while Figures 32 through 35 show some profiles of the jets and liners obtained from charges 22(c) through 22(f) respectively at the times indicated on the Figures.

33

Table I. Summary of the Computational Results.

CHARGES FIGURE 22	GEOMETRY					
	(a)	(b)	(c)	(d)*	(e)	(f)
Jet Mass (Kg) $\times 10^{3}$	11.7	11.6	11.8	9.6	12.6	18.3
Jet Tip Velocity (mm/μs)	6.4	3.6	5.0	6.1	6.8	5.7
Kinetic Energy of Jet (J) $\times 10^{-4}$	6.36	3.72	5.81	5.74	8.35	9.83
Total Liner Energy (J) $\times 10^{-5}$	1.68	0.89	1.63	1.17	1.94	2.90

The charge shown in Figure 22(d) has an iron flange 6.35 mm (0.25 in) thick to confine the expansion of the detonation products at the equatorial surface of the charge and delay the rarefaction emanating from that surface. The results of that computation are summarized in column 4 of Table 1, however those numbers listed are believed to be in error because parts of the jet flowed out of the computational mesh at the top transmittive boundary of the computational mesh before stablizing into a final state. Normally such a problem is avoided through constant monitoring of the calculations and a timely rezoning of the computational mesh. The numerical results given in column (d) should therefore be considered as lower bounds for this case. In the numerical simulation of the performance of this configuration, the detonation gases were not allowed to expand between the liner and the flange as it is the case in practice. It was observed in the computational model that the flange prevents the jet disruption by the liner's equator. Figure 33 shows the flow field configuration at t = 13.49μs.

The charge shown in 22(e) is similar to 22(a) but has a confining case on the outer surface of the charge. The jet obtained in this case has 31% more kinetic energy than the unconfined charge 22(a). The jet has a larger mass and a faster jet tip velocity. A larger portion of the explosive energy is communicated to the liner in this case. The results of this computation are summarized in column 5

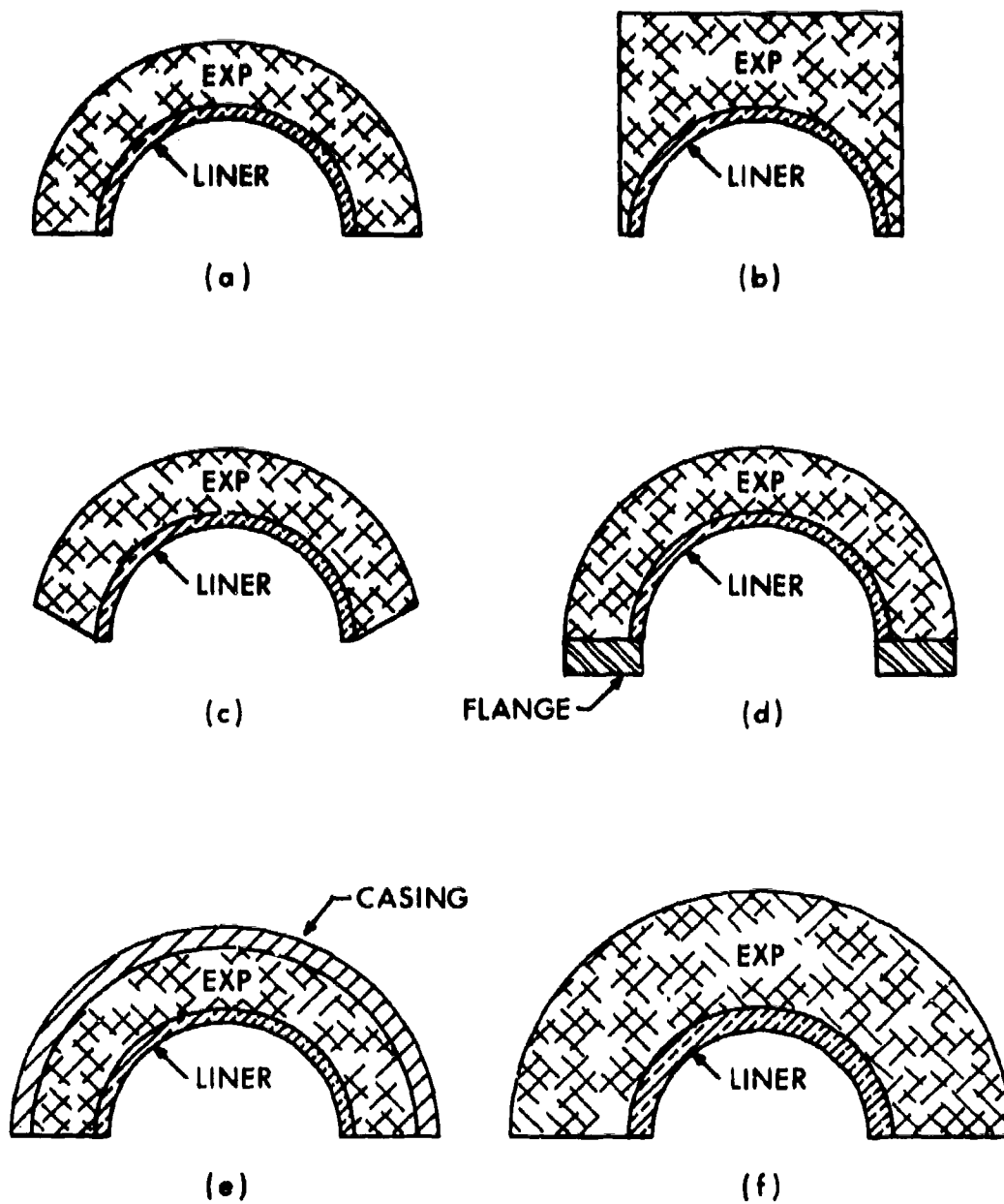*The results reported in this column are inaccurate due to a computational oversight.

34

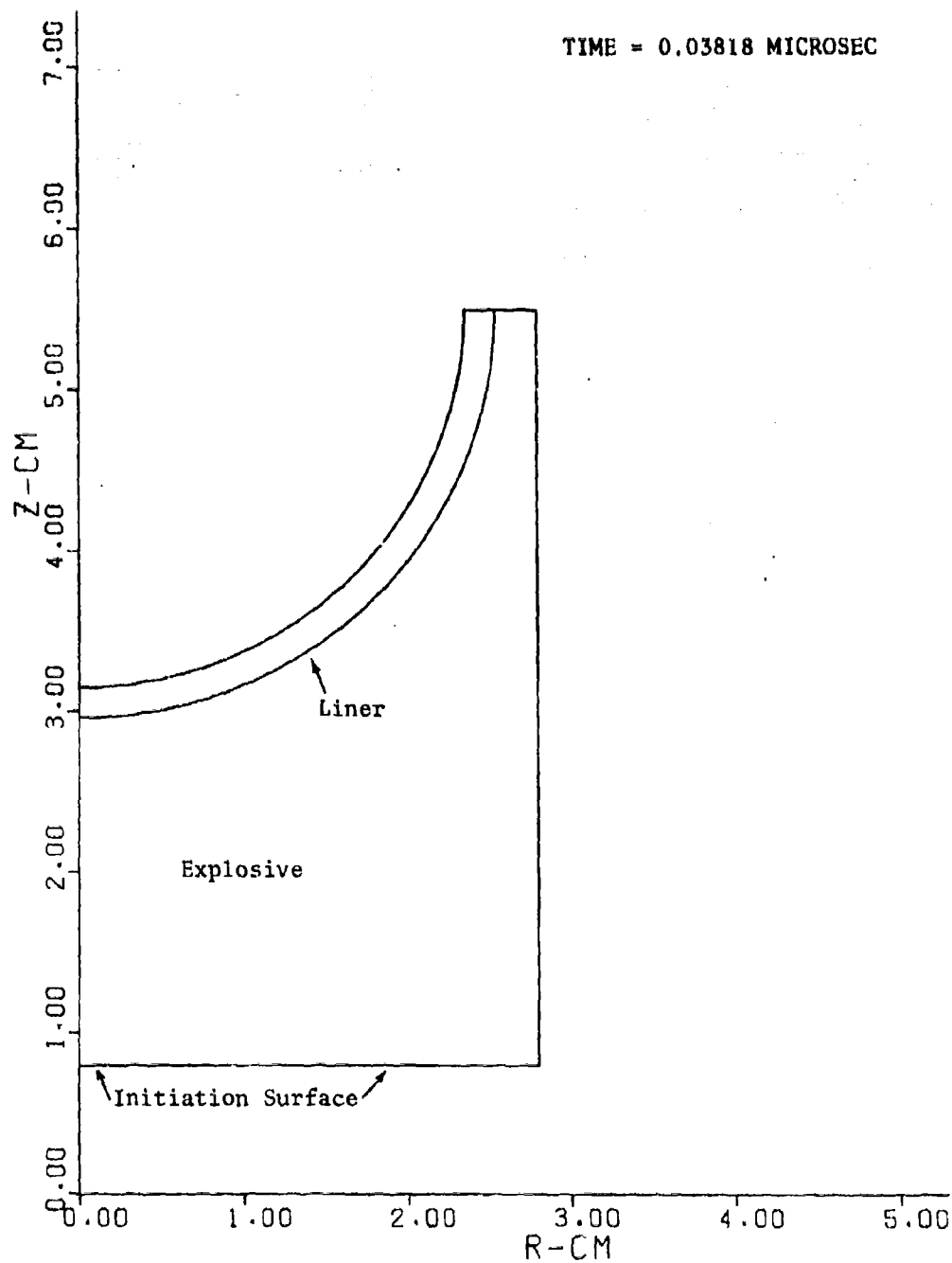Figure 22. Various Charge Configurations Studied

TIME = 0.03818 MICROSEC
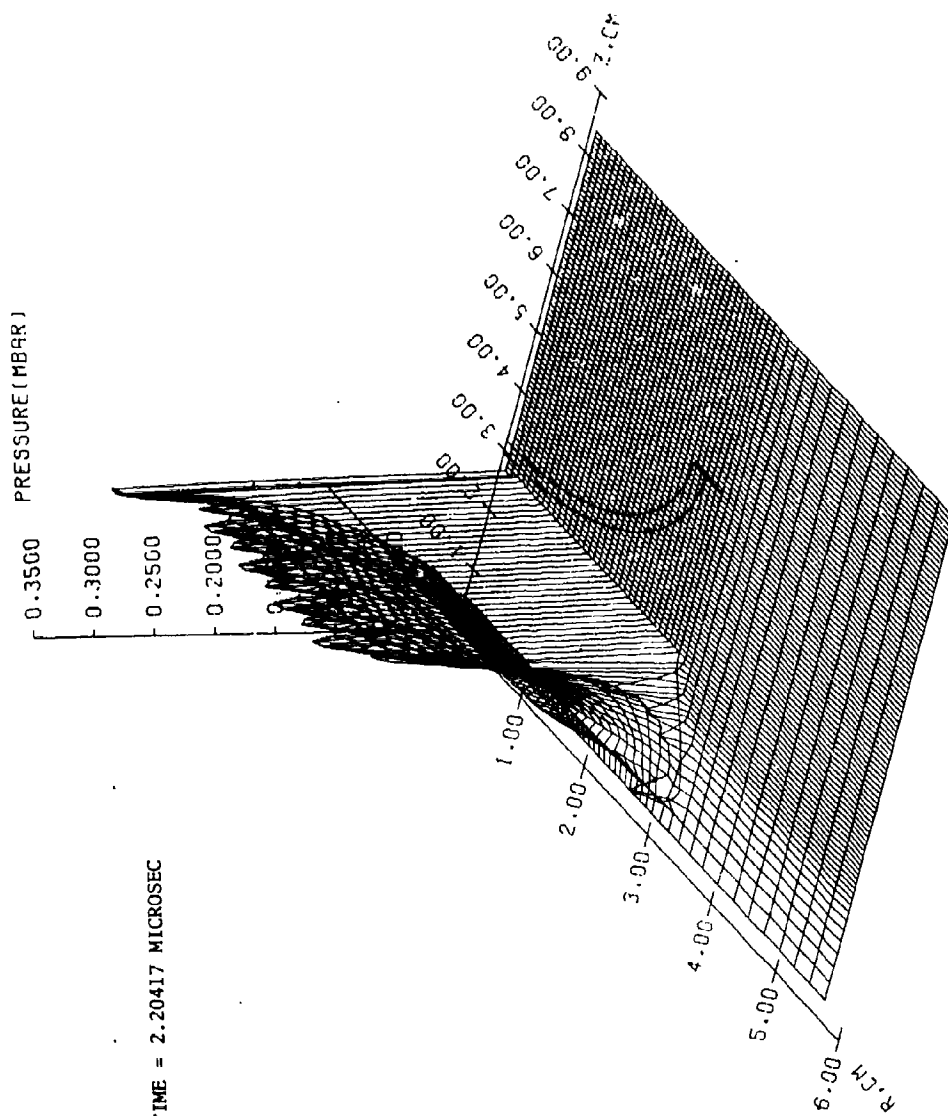

Figure 23.   Initial Computational Setup, Charge 22(b)

36

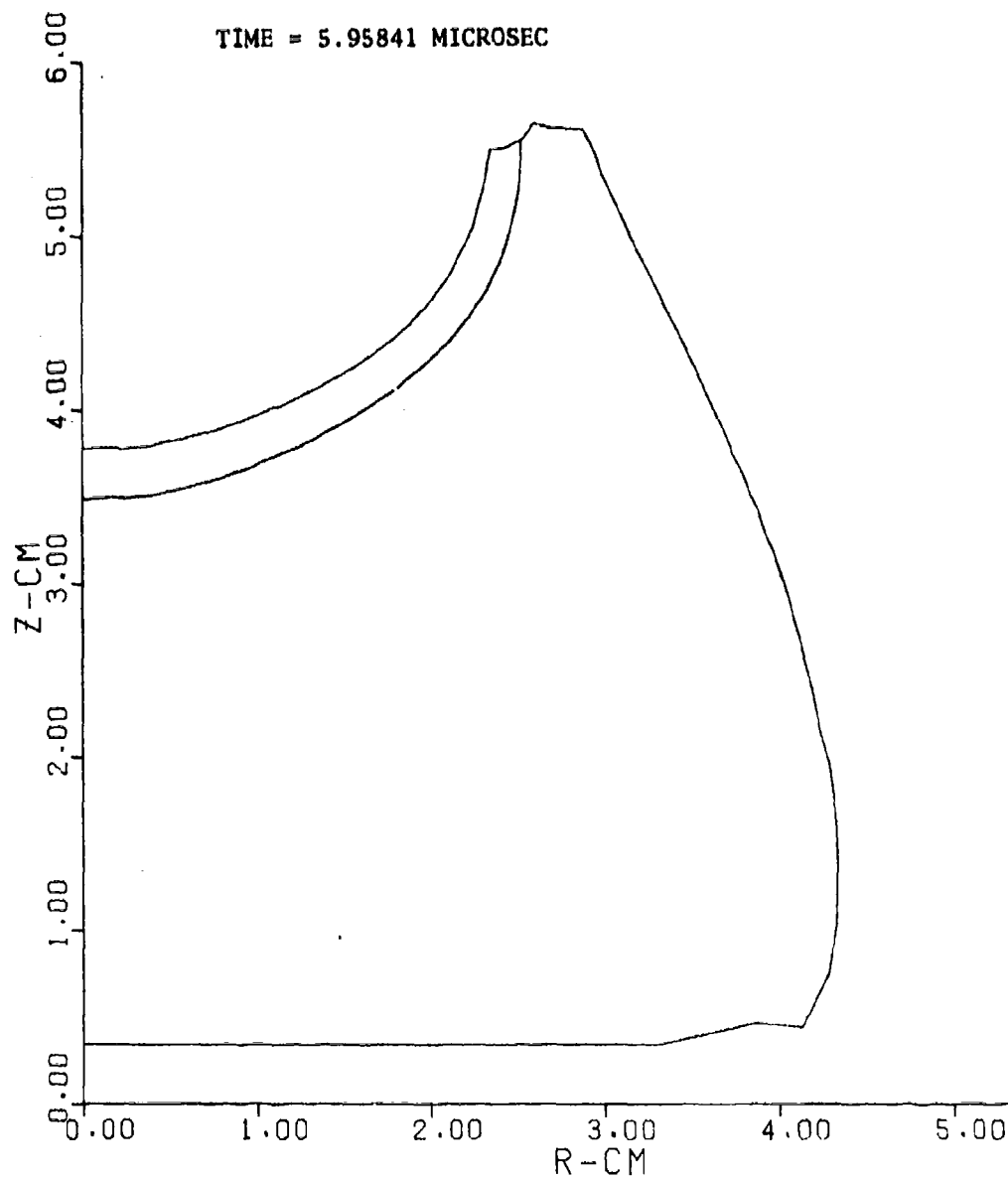Figure 24. The Plane Detonation Wave Before Striking the Liner Charge 22(b)

37

Figure 25. Early Stage of Liner Collapse, Charge 22(b)
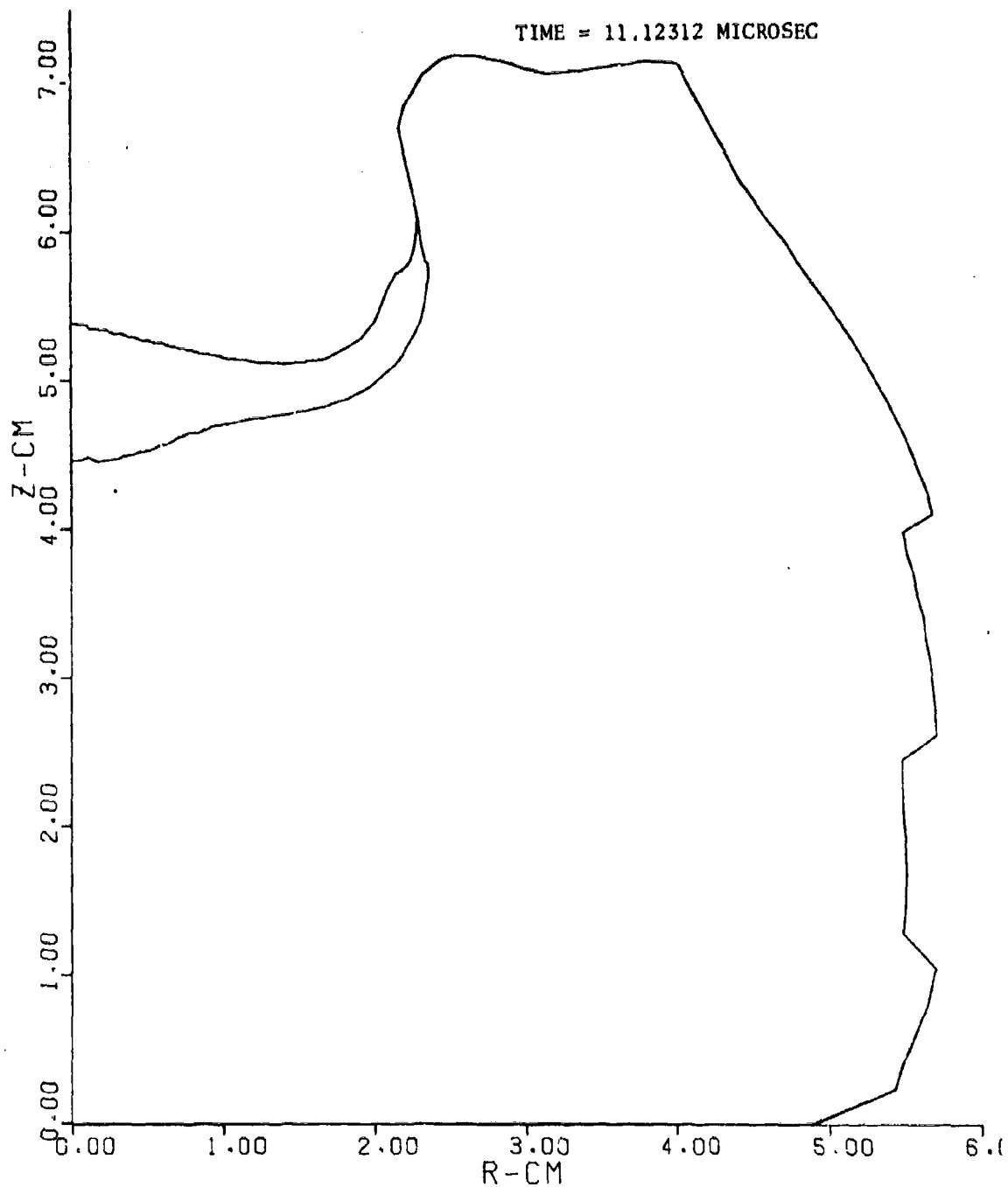
TIME = 11.12312 MICROSEC

Figure 26. Late Stage of Liner Collapse, Charge 22(b)

39

TIME = 12.87821 MICROSEC
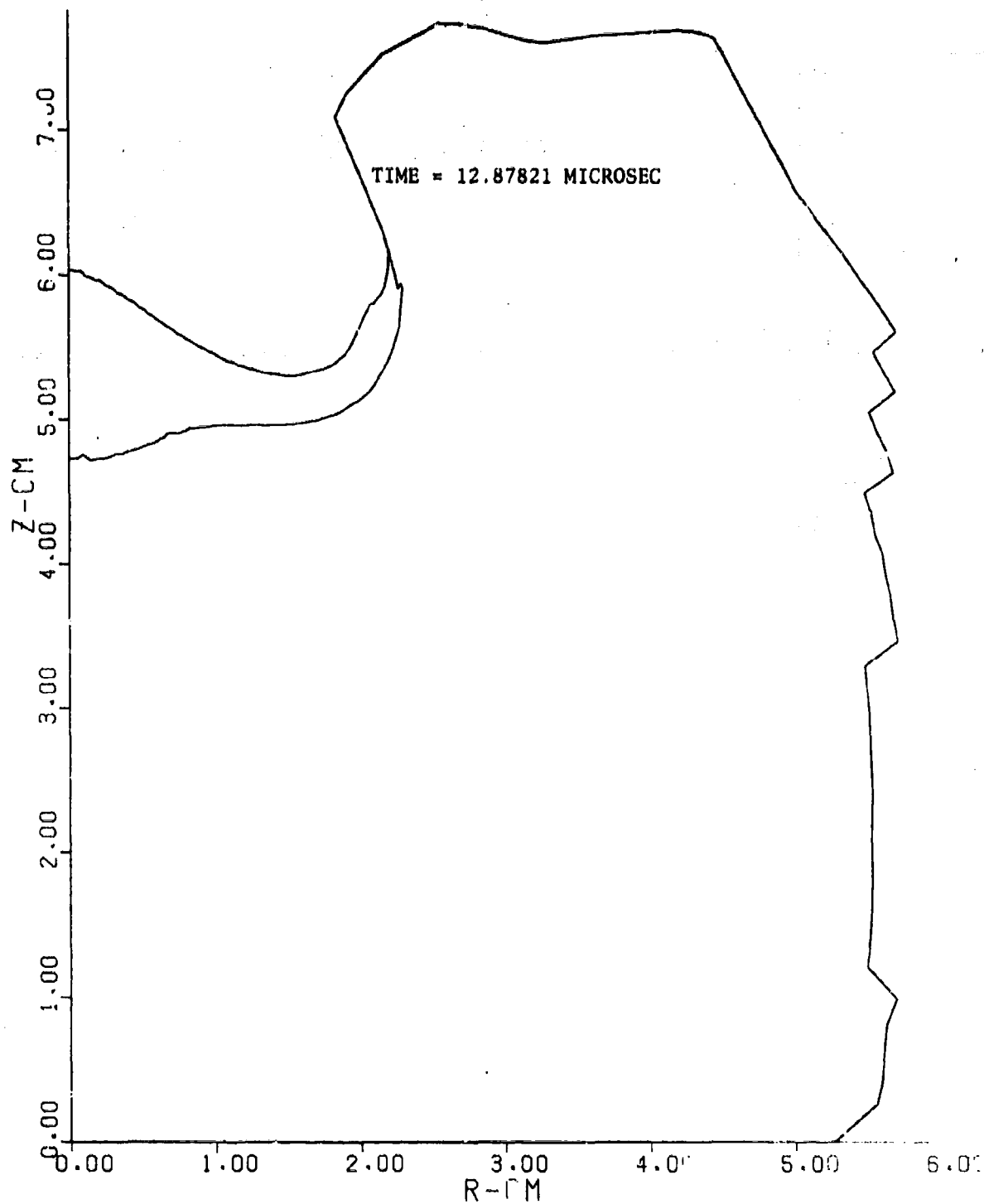
Figure 27. Early Stage of Jet Formation, Charge 22(b)

40

TIME = 14.23298 MICROSEC
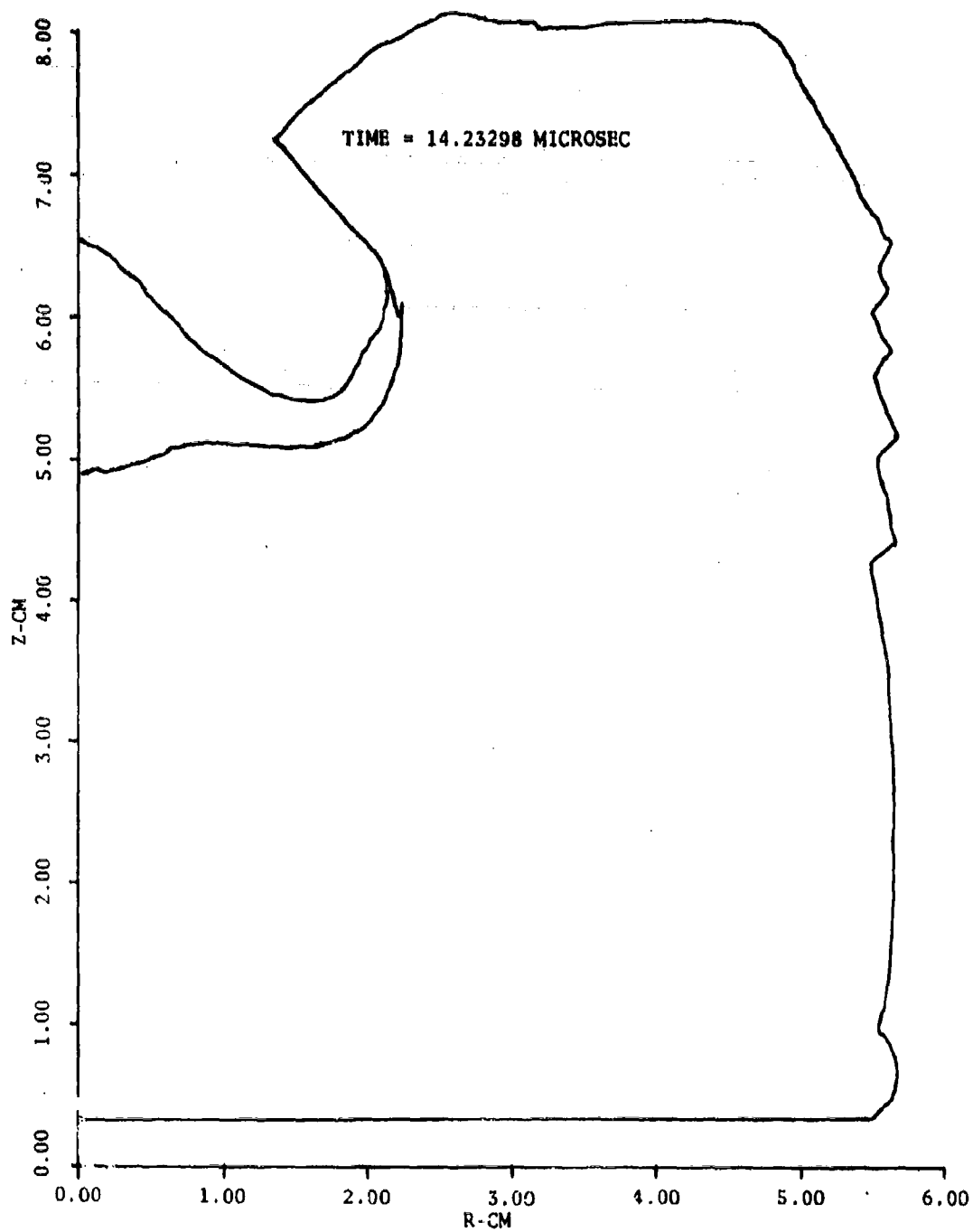
Figure 28. Jet Formation, Charge 22(b)

41

TIME = 18.23331 MICROSEC
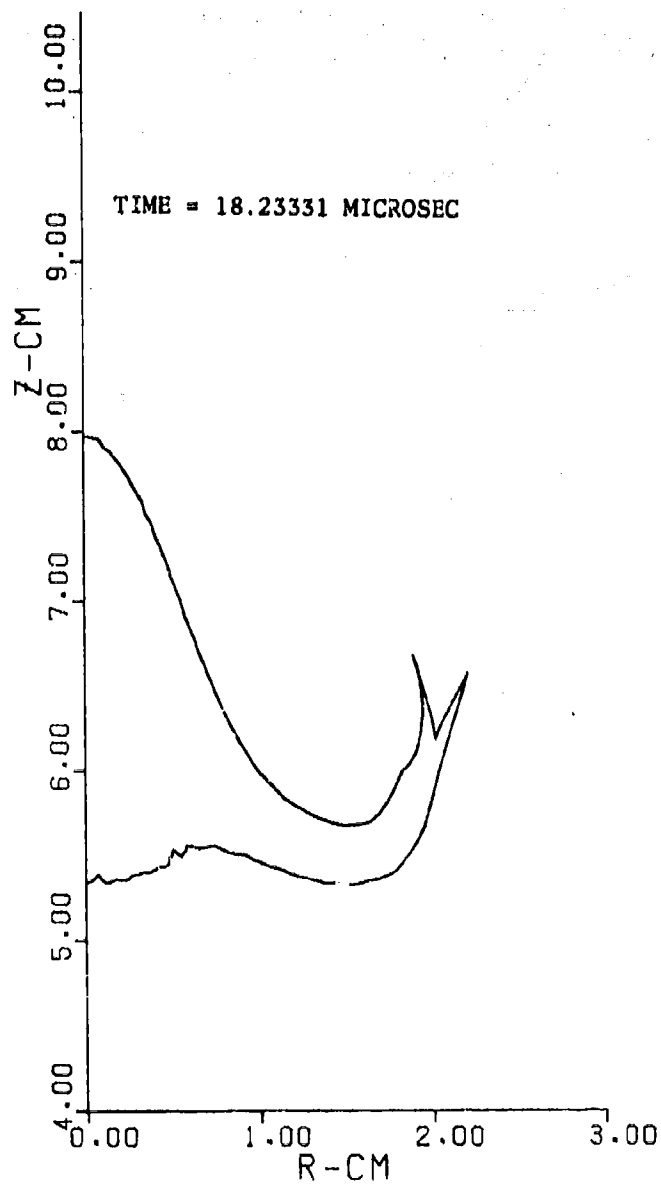
Figure 29.   Early Jet Elongation, Charge 22(b)

42
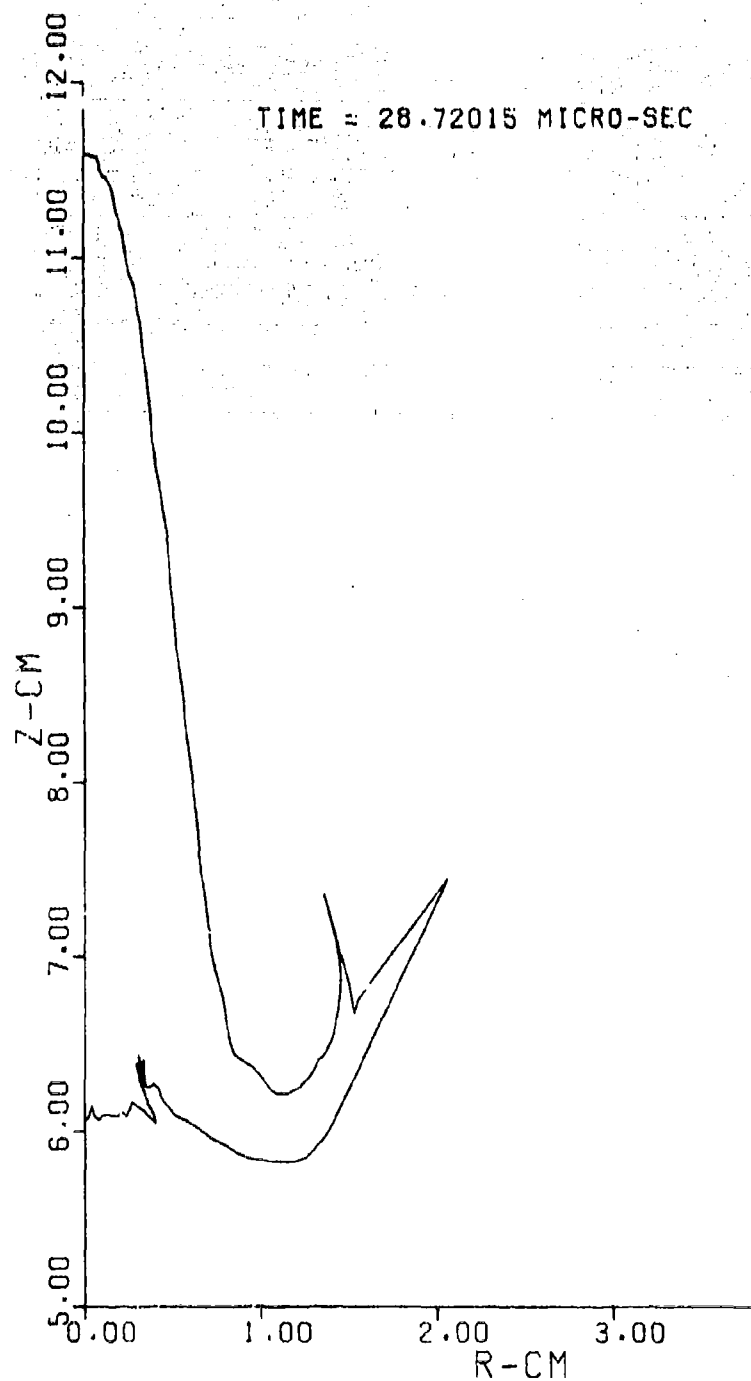
Figure 30.   Jet Elongation and Flight, Charge 22(b)

43

t = 0   25.0 μsec

(a)   (b)
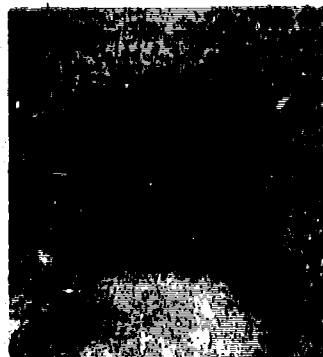
29.0 μsec
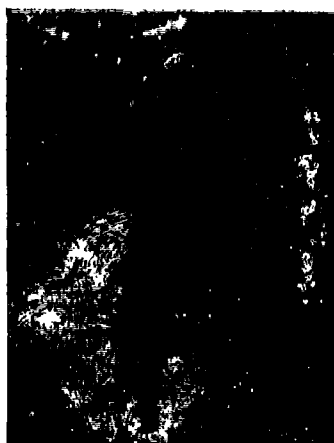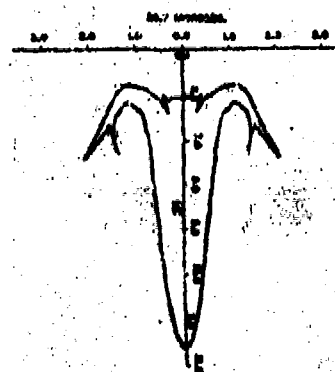
(c)   (d)

Figure 31. Comparison of Experimental and Computational Results,
Charge 22(b)

44

TIME = 15.33875 MICROSEC
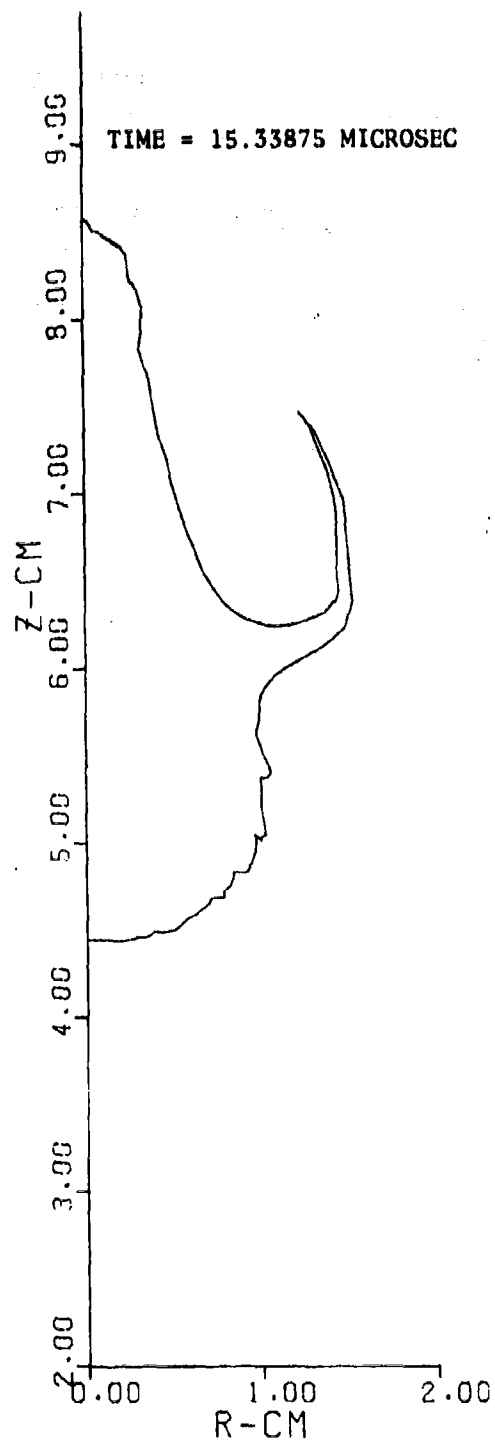
Figure 32. Jet and Liner Configuration, Charge 22(c)

45

TIME = 13.48655 MICROSEC
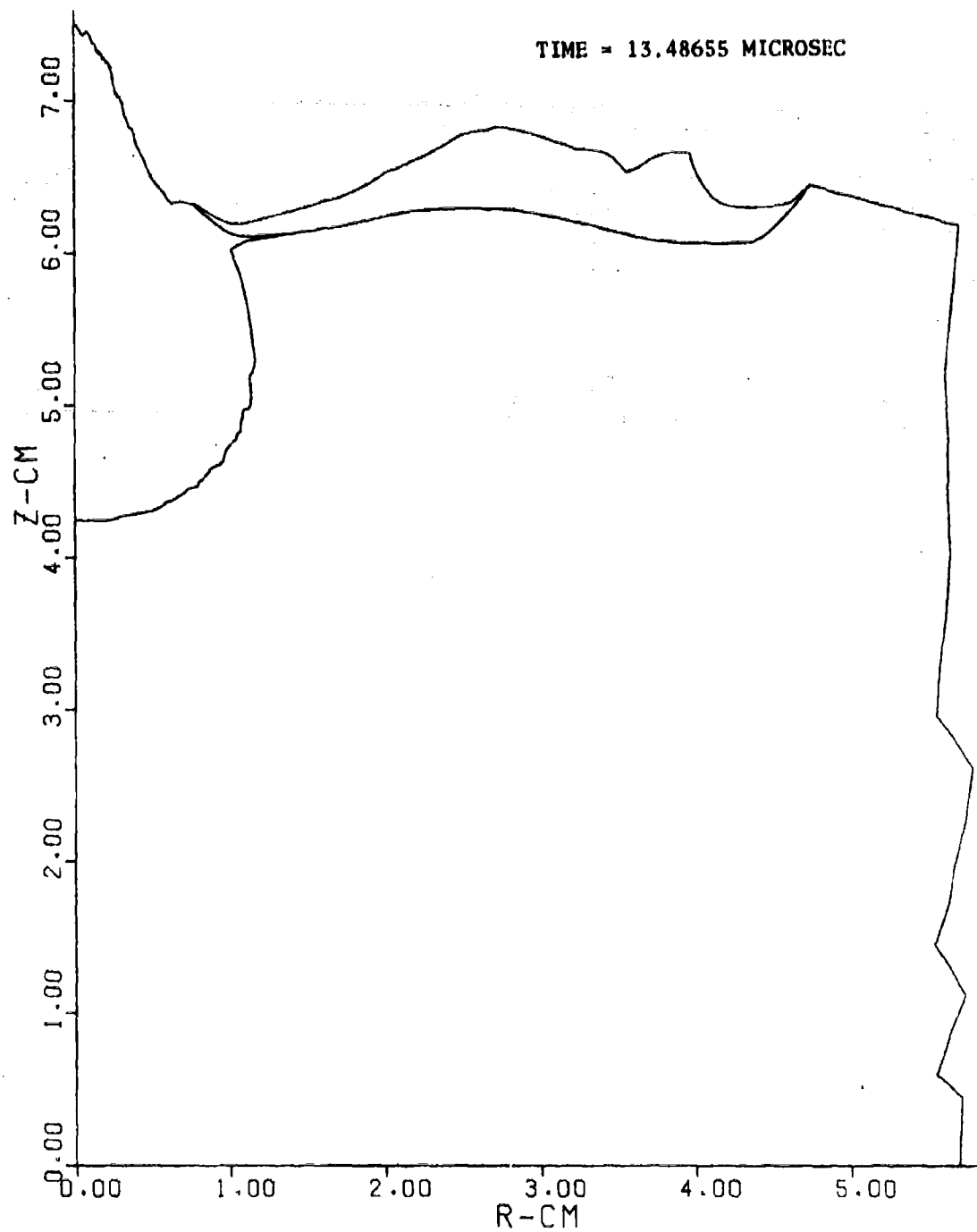
Figure 33.   Flow Field Configuration, Charge 22(d)

46

TIME = 12.84828 MICROSEC
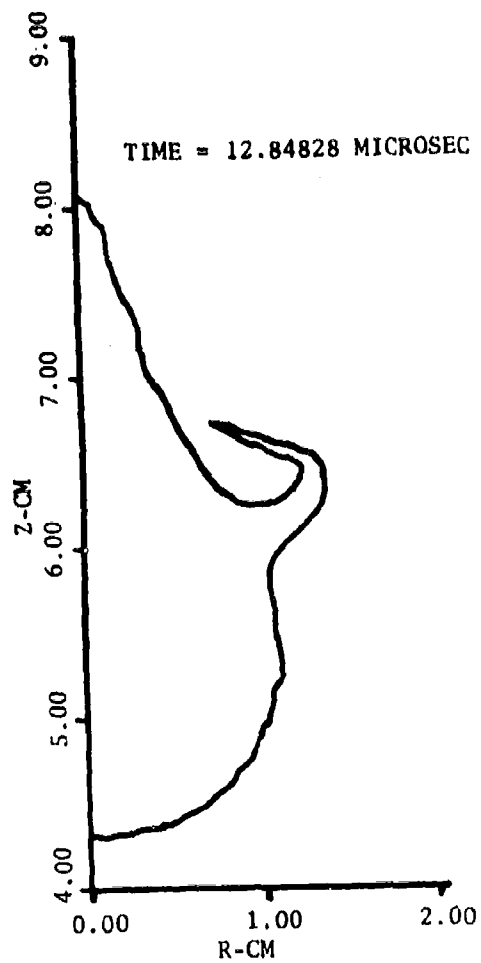
Figure 34.   Jet and Liner Configuration, Charge 22(e)

47

TIME = 13.01705 MICROSEC

Figure 35. Flow Field Configuration, Charge 22(f)

48

of Table 1. Unfortunately the equatorial section of the liner interrupts the jet at an early stage of its formation. Figure 34 shows the liner configuration at t = 12.85μs.

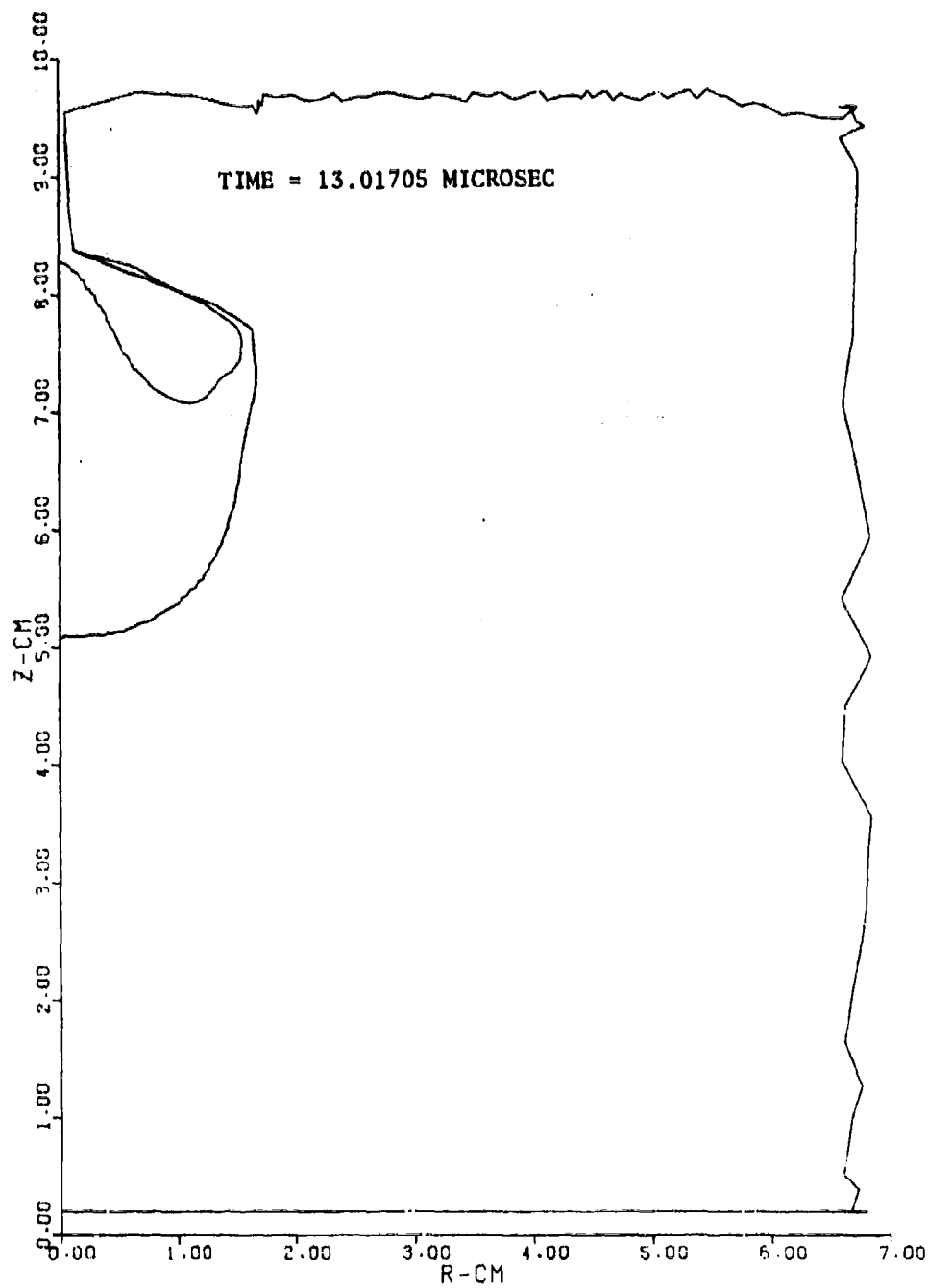The charge shown in 22(f) has a 3.81 mm (0.150 in) thick liner which is double the thickness of the liners used in the previous cases. The charge thickness was also increased to 24.13 mm (0.95 in). The initiation points were distributed over a 120° sector of the charge surface instead of the 180° hemispherical surface. The calculations revealed that the equatorial portion of the liner interrupts the jet about 18μs after initiation. The jet has more mass, but the jet tip velocity is slightly lower than case (a). A summary of the results in this case is given in column 6 of Table 1, and Figure 35 shows the flow field configuration in this case at t = 13.02μs.

VI. CONCLUSION

The above study explained the collapse and jet formation processes of a hemispherical liner with a hemispherical charge which is surface imploded. It is clear from the preceding study that the collapse and jet formation processes are fundamentally different from those of a cone. The various hemispherical liner elements converge towards a single point as they collapse. The jet forms due to the compression of liner material which squeezes out the jet materials as in an extrusion process. Conical liners collapse along a line. The study has shown that the jet originates from the inner surface layer of liner material. It has been shown that such jets have no inverse velocity gradients. The above study revealed the cause of the jet pinchoff as being due to the equatorial portion of the liner striking the jet. The design modifications discussed in Figures 22(c) and 22(d) alleviate this problem.

The second part of the study dealt with the effects of variations of the charge geometry and initiation mode as in charge 22(b) and dealt with the effects of confinement, and variations of the charge and liner thicknesses. The study of charge 22(b) revealed that the hemispherical liner turns inside out in this case and forms a short, thick, and slow moving jet which might be suitable for use against a certain class of targets.

In conclusion the above computational study has provided a wealth of quantitative values of various physical parameters most of which agree quite well with experimental measurements. This agreement in addition to the qualitative agreement of our computations with experimental results provides validation of our computational model and reveals the benefits of such studies as a design tool. In practice many experimental design parameters were based on similar hydrodynamic computations. Such computational studies can often be made quickly, economically and can result in considerable financial and time savings.

49

ACKNOWLEDGMENT

DISTRIBUTION LIST

No. of Copies	Organization	No. of Copies	Organization
12	Commander Defense Documentation Center ATTN: DDC-TCA Cameron Station Alexandria, VA 22314	3	Commander US Army Missile Research and Development Command ATTN: DRDMI-R Mr. B. Cobb Mr. R. Masucci Redstone Arsenal, AL 35809
1	Director of Defense Research and Engineering ATTN: Tech Lib, Rm 3D-1039 Washington, DC 20301	1	Commander US Army Tank Automotive Research & Dev Command ATTN: DRDTA-RWL Warren, MI 48090
1	Director Defense Advanced Research Projects Agency ATTN: Dr. Ernest F. Blaze 1400 Wilson Boulevard Arlington, VA 22209	2	Commander US Army Mobility Equipment Research & Development Command ATTN: Tech Docu Cen, Bldg. 315 DRSME-RZT Fort Belvoir, VA 22060
1	Commander US Army Materiel Development and Readiness Command ATTN: DRCDMA-ST 5001 Eisenhower Avenue Alexandria, VA 22333	1	Commander US Army Armament Materiel Readiness Command ATTN: DRSAR-LEP-L (Tech Lib) Rock Island, IL 61201
1	Commander US Army Aviation Research and Development Command ATTN: DRSAV-E 12th and Spruce Streets St. Louis, MO 63166	6	Commander US Army Armament Research and Development Command ATTN: Dr. N. Clark Mr. G. Randers-Pehrson Mr. J. Pearson Mr. J. Hershkowitz Mr. A. Anzalone Tech Lib Dover, NJ 07801
1	Director US Army Air Mobility Research and Development Laboratory Ames Research Center Moffett Field, CA 94035	1	Commander US Army Harry Diamond Labs ATTN: DRXDO-TI 2800 Powder Mill Road Adelphi, MD 20783
1	Commander US Army Electronics Command ATTN: DRSEL-RD Fort Monmouth, NJ 07703		

DISTRIBUTION LIST

No. of Copies	Organization	No. of Copies	Organization

3	Commander
	US Army Materials and
	  Mechanics Research Center
	ATTN: DRXMR-ATL, W. Woods
	        DRXMR-T, J. Mescall
	        Tech Lib
	Watertown, MA 02172
		2	Chief of Naval Research
			ATTN: Code 427
			        Code 470
			Department of the Navy
			Washington, DC 20325

1	Director
	US Army TRADOC Systems
	  Analysis Activity
	ATTN: ATAA-SL (Tech Lib)
	White Sands Missile Range
	NM 88002
		4	Commander
			US Naval Surface Weapons Center
			ATTN: Dr. H. Sternburg
			        Dr. Walker
			        Dr. J. Coughlin
			        Code 730, Lib
			Silver Spring, MD 20910

1	Assistant Secretary of
	  The Army (R&D)
	ATTN: Asst for Research
	Washington, DC 20310
		2	Commander
			US Naval Surface Weapons Center
			ATTN: Code DG-50, K.Bannister
			        Tech Lib
			Dahlgren, VA 22448

2	HQDA (DAMA-ZA; DAMA-AR) Washington, DC 20310	1	Commander US Naval Weapons Center ATTN: Code 45, Tech Lib China Lake, CA 93555
1	Commander US Army Research Office P. O. Box 12211 Research Triangle Park NC 27709	1	Commander US Naval Research Laboratory Washington, DC 20375
2	Commander US Naval Air Systems Command ATTN: Code AIR-310 Code AIR-350 Washington, DC 20360	1	USAF/AFRDDA Washington, DC 20330
1	Commander US Naval Ordnance Sys Command ATTN: Code ORD-0332 Washington, DC 20360	1	AFSC/SDW Andrews AFB Washington, DC 20331
		1	US Air Force Academy ATTN: Code FJS-RJ (NC) Tech Lib Colorado Springs, CO 80840
		1	AFATL/DLJW, Mr. Beech Eglin AFB, FL 32542

52

DISTRIBUTION LIST

No. of Copies	Organization	No. of Copies	Organization

1 AFWL (SUL, LT Tennant)
Kirtland AFB, NM 87116

1 AFAL/AVW
Wright-Patterson AFB, OH 45433

1 AFLC/MMWMC
Wright-Patterson AFB, OH 45433

1 Director
US Bureau of Mines
ATTN: Mr. R. Watson
4800 Forbes Street
Pittsburgh, PA 15213

6 Director
Lawrence Radiation Laboratory
ATTN: Dr. M. Wilkins
      Dr. J. Kury
      E. D. Giroux
      Dr. E. Lee
      Dr. H. Hornig
      Tech Lib
P. O. Box 808
Livermore, CA 94550

1 Director
National Aeronautics and
  Space Administration
Langley Research Center
Langley Station
Hampton, VA 23365

1 Director
National Aeronautics and
  Space Administration
Lewis Research Center
2100 Brookpark Road
Cleveland, OH 44135

1 Lockheed Missiles and
  Space Company
ATTN: Mr. J. E. May
      55-80 Bldg. 57
P. O. Box 504
Sunnyvale, VA 94088

2 Physics International Corp
ATTN: Dr. C. Godfrey
      L. Berhaman
2700 Merced Street
San Leandro, CA 94577

2 Sandia Laboratories
ATTN: Dr. W. Herrman
      Dr. L. Bertholf
Albuquerque, NM 87115

1 Shock Hydrodynamics
ATTN: Dr. L. Zernow
4710-4716 Vineland Avenue
North Hollywood, CA 91602

1 Systems, Science & Software
ATTN: Dr. R. Sedgwick
P. O. Box 1620
La Jolla, CA 92037

2 Drexel Institute of Technology
Wave Propagation Research Ctr
ATTN: Prof. P. Chou
      Dr. J. Carleone
32nd & Chestnut Streets
Philadelphia, PA 19104

1 Stanford Research Institute
ATTN: Dr. A. Florence
Poulter Laboratories
Menlo Park, CA 94025

DISTRIBUTION LIST

No. of Copies	Organization

3   University of California
Los Alamos Scientific Lab
ATTN: Dr. R. Karpp
           Dr. J. Walsh
           Tech Lib
P. O. Box 1663
Los Alamos, NM   87545

1   Washington State University
Department of Physics
ATTN: Prof. G. Duvall
Pullman, WA   99163

Aberdeen Proving Ground

     Marine Corps Ln Ofc
     Dir, USAMSAA